Capacity-Contribution Paradox: Fatty Acid Oxidation Compensates for Low Glucose-Derived Acetyl-CoA in Cancer.

Nancy T Santiappillai[1,†], Xiangwen C Kong[1], Mariam F Hakeem-Sanni[1], Masih Ghasemi[1], Anabel Withy[1], Lake-Ee Quek[2], Andrew J Hoy[1,*]

[1] School of Medical Sciences, Charles Perkins Centre, The University of Sydney, Sydney, New South Wales 2006, Australia.

[2] School of Mathematics and Statistics, Charles Perkins Centre, The University of Sydney, Sydney, New South Wales 2006, Australia.

[*] Contact. Tel: +61 2 9351 2514; Email: andrew.hoy@sydney.edu.au

[†] Current address. Radiology, and Molecular Pharmacology Program, Memorial Sloan Kettering Cancer Center, New York, New York, United States of America.

Word count: 6279 words

Abstract

Upregulated fatty acid oxidation (FAO) is a hallmark of many aggressive cancers and is widely presumed to fuel the tricarboxylic acid (TCA) cycle for ATP production. However, the quantitative relationship between FAO capacity and its contribution to mitochondrial metabolism relative to other fuels remains unclear. Here, we combined parallel stable-isotope tracing with metabolic phenotyping across a diverse panel of 27 cancer cell lines to reveal a fundamental capacity-contribution paradox. Despite exhibiting FAO rates that varied over eight-fold, exogenous long-chain fatty acids consistently contributed minimally (<10%) to TCA cycle intermediates in all cancer cell lines. We demonstrated that FAO functions as a compensatory source of acetyl-CoA in cells with limited glucose-derived acetyl-CoA synthesis, rather than acting as a primary fuel source. In this context, high FAO rates do not primarily result from FAO-mediated suppression of glucose oxidation, but instead reflect the recruitment of fatty acid- and glutamine-derived carbons via a malic enzyme-dependent shunt to sustain the mitochondrial acetyl-CoA pool while preserving glucose-derived anaplerotic flux. These findings challenge the prevailing view that FAO serves as a primary bioenergetic fuel in cancer, instead identifying it as a compensatory rheostat that supplements acetyl-CoA supply in glucose-limited settings by working together with glutamine-driven, malic enzyme-dependent anaplerosis, providing a mechanistic framework to reinterpret the efficacy of FAO inhibitors beyond simple caloric starvation.

Keywords

Mitochondria, fatty acid oxidation, acetyl-CoA metabolism, glutamine shunt, TCA cycle, cancer metabolism.

Introduction

The integration of diverse substrates characterises cellular metabolism. Historically, glucose and glutamine have been the focal points of metabolic research in oncology, and are recognised as primary fuel sources and biosynthetic substrates [1-3]. However, these pathways do not function in isolation; instead, they interact within an interconnected metabolic network, regulated by mitochondrial function, redox states, and nutrient sensing, among other mechanisms [4]. Metabolic plasticity, the capacity of cancer cells to flexibly reprogram energy production and biosynthetic processes in response to changing environmental and intracellular cues, underpins both tumour survival and therapeutic resistance [5,6]. This plasticity is intricately linked to the tricarboxylic acid (TCA) cycle, in which glucose-derived pyruvate, glutamine-derived oxoglutarate, and fatty acid-derived acetyl-CoA converge as central metabolic nodes [4]. Understanding how these substrates compete for entry into the TCA cycle and how their utilisation is coordinated by mitochondrial biology remains profoundly underappreciated, even though this integration is central to the cancer cell phenotype and disease progression.

Fatty acid oxidation (FAO) and its interaction with mitochondrial glucose and glutamine metabolism exemplify this mechanistic gap. Genes encoding FAO enzymes are frequently upregulated in diverse cancer types, including glioma[7], prostate[8] and lung cancers[9], and pharmacological inhibition of carnitine palmitoyltransferase 1 (CPT1), the rate-limiting enzyme controlling mitochondrial fatty acid entry[10], reduces ATP production and cancer cell viability in multiple malignancies[11-18]. However, these studies presume that upregulated FAO capacity directly translates into substantial TCA cycle fuelling and bioenergetic output, an assumption rooted in classical biochemistry textbooks rather than empirical validation in cancer cells. Critically, previous investigations into cancer cell FA metabolism, including FAO, typically examined these pathways in isolation, often lacking quantitative measures of concurrent glucose or glutamine oxidation [19-23]. Thus, they failed to account for substrate

competition and metabolic plasticity, which determine whether FAO serves as a major carbon source for the TCA cycle or plays alternative metabolic roles. Collectively, these findings reveal a critical gap in our understanding of cancer metabolism: the quantitative relationship between FAO capacity and its contribution to central carbon flux relative to other major fuels, such as glucose and glutamine.

Here, we address this gap through an integrated multimodal approach combining parallel stable isotope tracing, quantitative assessment of mitochondrial biology, and metabolic correlation studies across a diverse panel of cancer cell lines spanning ten tissue origins with heterogeneous FAO capacity. Our analysis revealed a fundamental complexity in mitochondrial substrate utilisation, with exogenous long-chain fatty acids contributing minimally (<10%) to TCA cycle intermediate pools compared to glucose (30–50%) and glutamine (20–45%), despite FAO rates ranging over eight-fold among our pan-cancer cell panel. This paradox of capacity versus contribution was resolved by identifying that cells with faster FAO rates exhibit coordinated metabolic reorganisation, in which low glucose-derived acetyl-CoA synthesis is supplemented by increased recruitment of fatty acid- and glutamine-derived carbons, while glucose-derived anaplerosis is preserved. These findings suggest that FAO functions not as a static bioenergetic input but as a dynamic metabolic rheostat within an integrated network, where mitochondrial functional states tune acetyl-CoA supply by coupling fatty acid oxidation to glutamine-driven, malic enzyme-dependent acetyl-CoA production. By defining distinct functional metabolic states characterised by unique isotope-labelling signatures and mitochondrial phenotypes, we establish a quantitative framework for understanding metabolic heterogeneity as a determinant of cancer cell phenotype and therapeutic vulnerability, with implications for precision oncology and metabolic phenotyping strategies.

Results

Fatty acid oxidation in cancer cells showed diverse rates and spare capacity.

To investigate the role of fatty acids in cancer metabolism, it is essential first to establish the baseline capacity of diverse tumour lineages to oxidise fatty acids. We first screened a panel of 27 cancer cells from 10 different origins (Figure 1A) for basal FAO rates using [1-^{14}C]-palmitate and measuring CO2 production, revealing remarkable heterogeneity. In general, prostate cancer cells exhibited some of the highest FAO rates among the cancer types (Figure 1B).

Next, we sought to gain insights into the dynamic range, or plasticity, of FAO, and thereby the "spare capacity" of this pathway to ramp up flux in response to stress. It has been shown that FAO rates increase in response to glucose metabolism inhibition in glioblastoma and breast cancer cells [24,25]. As such, we quantified FAO rates in glucose-free conditions and termed this the maximal FAO rate. As predicted, glucose withdrawal triggered a universal upregulation of FAO across all cancer lines tested (Figure 1C and S1A), with increases ranging from 2-fold to > 8-fold. Based on the fold change in maximal and basal FAO rates as a measure of relative FAO spare capacity, we selected six cell lines that ranged from high (> 4-fold), mid (2-4-fold), and low (0-2-fold) FAO spare capacity: MDA-MB-231 and MCF-7 (breast), MIA PaCa-2 (pancreatic), DO4 (melanoma), HEPG2 (liver), and HT-29 (colorectal) (Figure 1D). We further explored the relationship between FAO rates and media glucose levels in this panel of cells and determined that FAO is actively suppressed by glucose levels of 3 mM or greater (Figure S1B and S1C). Conversely, FAO was not dependent on nutrient gradients since a 5-fold increase in media palmitate (0.1 mM to 0.5 mM) did not increase FAO rate in the presence of 5 mM glucose (Figure S1D). These data are consistent with a model in which FAO is preferentially

engaged when glucose utilisation is limited, either by availability or intrinsic constraints on glucose-derived acetyl-CoA synthesis.

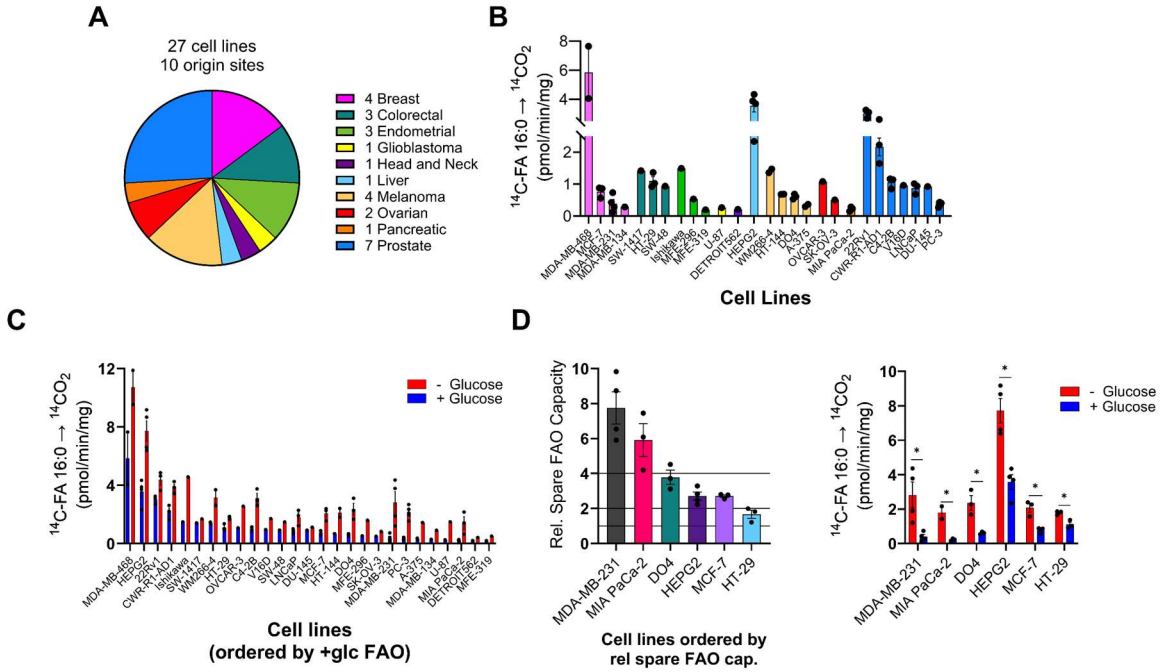

Figure 1. Cancer cells exhibit heterogeneous fatty acid oxidation rates and distinct metabolic spare capacities in response to glucose availability.

(A) Panel of 27 cancer cell lines from 10 tissue origin sites measured for FAO capacity.
(B) Basal [1-^{14}C]-FA 16:0 oxidation rates in the presence of 5 mM glucose. Cells ordered by cancer origin site. N=1-5 per cell line.
(C) [1-^{14}C]-FA 16:0 oxidation rates in the presence (5 mM; blue) or absence of glucose (red). N=1-5 per cell line.
(D) Selection of 6 cell lines based on relative spare FAO capacity (maximal FAO rate/basal FAO rate) differences (<2 to >7; left) between maximal FAO rate (- glucose) and basal FAO rate (+ glucose; right). N=3-4 per cell line.

Graphs show mean ± SEM. * $P < 0.05$ by Student t-test. See also Figure S1.

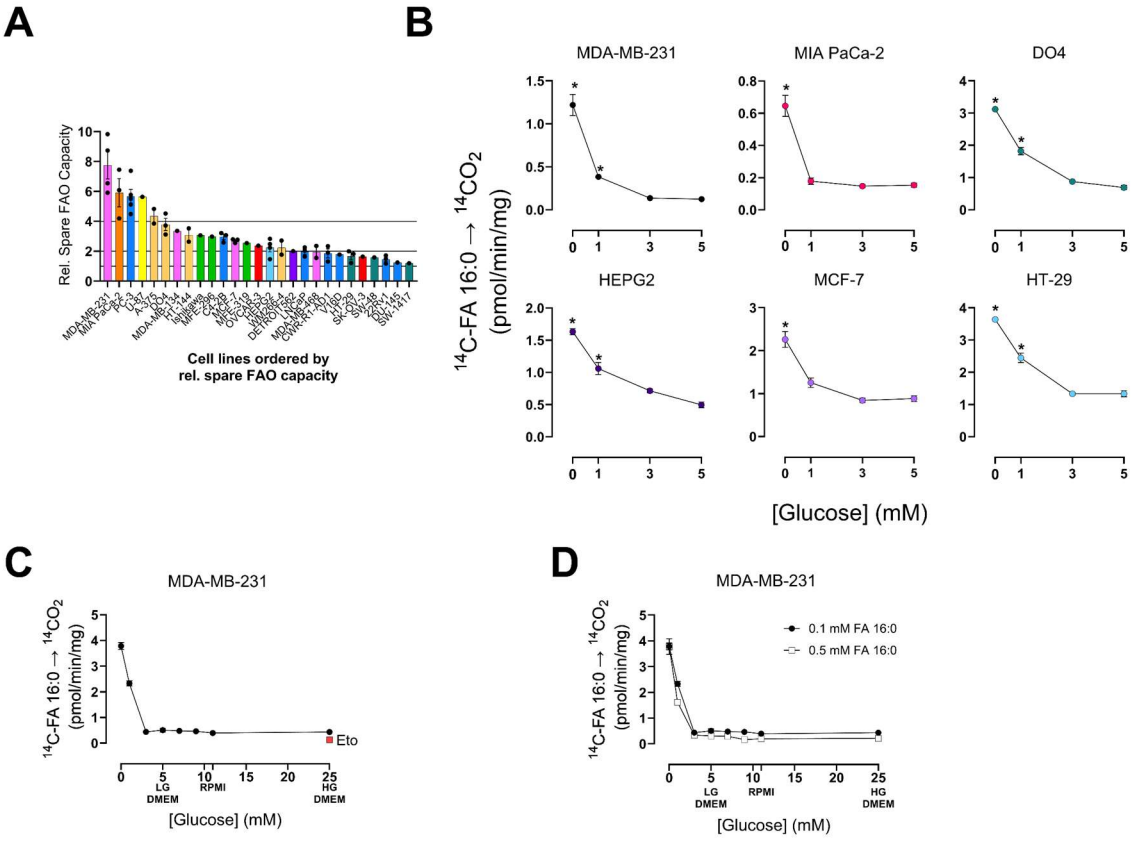

Figure S1, related to figure 1. Glucose availability suppresses fatty acid oxidation rates across diverse cancer lineages.

(A) Relative spare FAO capacity of cancer cells determined as [1-^{14}C]-FA 16:0 (palmitate) oxidation rates in the absence of glucose (maximal FAO rate) divided by [1-^{14}C]-FA 16:0 oxidation rates in the presence of 5 mM glucose (basal FAO rate). Cell lines ranked by fold change magnitude. N=1-5 per cell line.
(B) [1-^{14}C]-FA 16:0 oxidation rates in the presence of 5 mM, 3 mM, 1 mM, or 0 mM glucose. N=3 per cell line. * $P < 0.05$ vs 5 mM glucose by One-way ANOVA with Dunnett's multiple comparisons test.
(C) [1-^{14}C]-FA 16:0 oxidation rates in MDA-MB-231 cells in the presence of 0 to 25 mM glucose, or 25 mM + 10 μM etomoxir, in 0.1mM ^{14}C-FA 16:0. N=1 with 3 technical replicates.
(D) [1-^{14}C]-FA 16:0 oxidation rates in MDA-MB-231 cells in the presence of 0 to 25 mM glucose in 0.1 mM FA 16:0 compared to 0.5 mM FA 16:0. N=1 with 3 technical replicates.

Graphs show mean ± SEM.

Palmitate is a minor TCA cycle carbon source compared to glucose and glutamine.

Next, we used a parallel tracing strategy that fed cells uniformly labelled with ^{13}C-glucose, glutamine, or palmitate (FA 16:0) to gain new insights into the quantitative contributions of enrichment to TCA cycle intermediates in our subset of six cell lines spanning FAO spare capacity (Figure 2A). We first identified that 6 hours was the optimal tracing duration, as media substrate levels were not fully depleted and there was no evidence of impaired substrate uptake (Figure S2A). This was critical because we showed that removal or very low levels of extracellular glucose had a striking effect on FAO rates (Figure 1). As such, the depletion of glucose from the media after 12 and 24 hours likely affects ^{13}C-palmitate metabolism and enrichment patterns. This rapid rate of media glucose consumption can somewhat be avoided by doubling the media volume (Figure S2B).

We used m+2 acetyl-CoA from U-^{13}C-palmitate as our stable-isotope measure of FAO (Figure 2B), which, as expected, positively correlated with basal FAO rate (r = 0.77; Figure 2C), as determined using ^{14}C-palmitate tracing (Figure 1). However, basal FAO rate did not correlate with ^{13}C-palmitate enrichment of other TCA cycle intermediates (Figure S2C). The fractional contribution of ^{13}C-palmitate to m+2 acetyl-CoA did positively correlate with maximal FAO rate (glucose-free media; Figure S2D), not with the absolute FAO spare capacity (delta between maximal and basal FAO rate; Figure S2E), but interestingly, there was a negative correlation with the relative FAO spare capacity (maximal FAO/basal FAO; Figure S2F). These observations suggest that cells with high basal FAO (and high m+2 acetyl-CoA from palmitate) operate closer to their mitochondrial FAO ceiling and exhibit limited relative plasticity for FAO upregulation. In contrast, low-basal FAO cells retain greater proportional reserve capacity despite lower absolute rates. Critically, these data highlight that basal FAO rate does not predict

157 the FAO rate or capacity in other settings and that there is significant heterogeneity in both
158 relative and absolute FAO spare capacity in cancer cells.

159 These patterns of fatty acid metabolism in our panel of cancer cells were, in part, explained by
160 features of mitochondrial biology. Cells with higher basal FAO rates had greater CPT1A
161 protein levels (Figure 2D and S2G), but this did not predict maximal FAO capacity or the
162 relative spare capacity of the cells, as there was no relationship between CPT1A protein levels
163 and maximal FAO capacity or relative spare capacity (Figure S2H). In fact, cells with greater
164 relative spare FAO capacity had lower CPT1 protein levels (r = -0.665, P = 0.013; Figure 2H).
165 This distinction is vital for interpreting therapeutic targets; inhibition of CPT1A may have
166 disproportionate effects depending on whether a tumour is operating at basal or maximal
167 capacity. Furthermore, cells with high FAO rates frequently exhibited lower mitochondrial
168 mass (quantified using MitoTracker Green; Figure S2H). Finally, there was no relationship
169 between measures of FAO and mitochondrial membrane potential, determined using
170 MitoTracker Red (normalised to MitoTracker Green; Figure S2H). These data imply that high
171 basal FAO flux is achieved through higher CPT1 protein levels and likely greater efficiency,
172 rather than through global mitochondrial biogenesis.

173 A notable outcome of the U-^{13}C-palmitate tracing experiments was the very low enrichment of
174 acetyl-CoA and TCA cycle metabolites, with palmitate minimally contributing 9-18% of
175 carbons to acetyl-CoA (Figure 2B), and <6% to TCA cycle metabolites citrate, oxoglutarate
176 and malate, compared to glucose (30-50%) and glutamine (20-45%) (Figure 2E). This is, even
177 though FAO is commonly assumed to be a major contributor to the TCA cycle by producing
178 acetyl-CoA and reducing equivalents to support ATP production [26,27]. This low rate of
179 enrichment of acetyl-CoA, citrate and other TCA cycle intermediates was not due to low
180 precursor enrichment (>56% enrichment of palmitoyl-carnitine from ^{13}C-palmitate) (Figure

181 2F), nor did differences in precursor labelling explain differences in the contribution of glucose
182 and glutamine; >80% enrichment of pyruvate from ^{13}C-glucose, and >60% enrichment of
183 intracellular glutamine from extracellular ^{13}C-glutamine (Figure 2F). Furthermore, this low
184 enrichment was also observed with other FAs that varied in saturation (double bonds) and
185 carbon chain lengths; specifically [U-^{13}C]-stearate (FA 18:0), oleate (FA 18:1), linoleate (FA
186 18:2), and linolenate (FA 18:3). In all experiments, each ^{13}C-FA enriched their direct acyl-
187 carnitine counterpart species by a fractional ratio of 0.5-0.95 (Figure S2I), and exogenous
188 LCFAs contributed <10% of labelled carbons to citrate, oxoglutarate, or malate (Figure S2J).
189 Collectively, these data further demonstrate that exogenous long-chain fatty acids, regardless
190 of saturation status or chain length, are minor carbon sources for the TCA cycle across a pan-
191 cancer panel of cells spanning a range of FAO rates and spare capacities. As such, these
192 findings directly challenge the fuel hypothesis of the role of FAO in cancer cells, because if
193 FAO accounts for a significant portion of oxygen consumption but provides <10% of the TCA
194 cycle carbon, the pathway cannot serve as the primary source of biomass or bioenergetic
195 carbon.

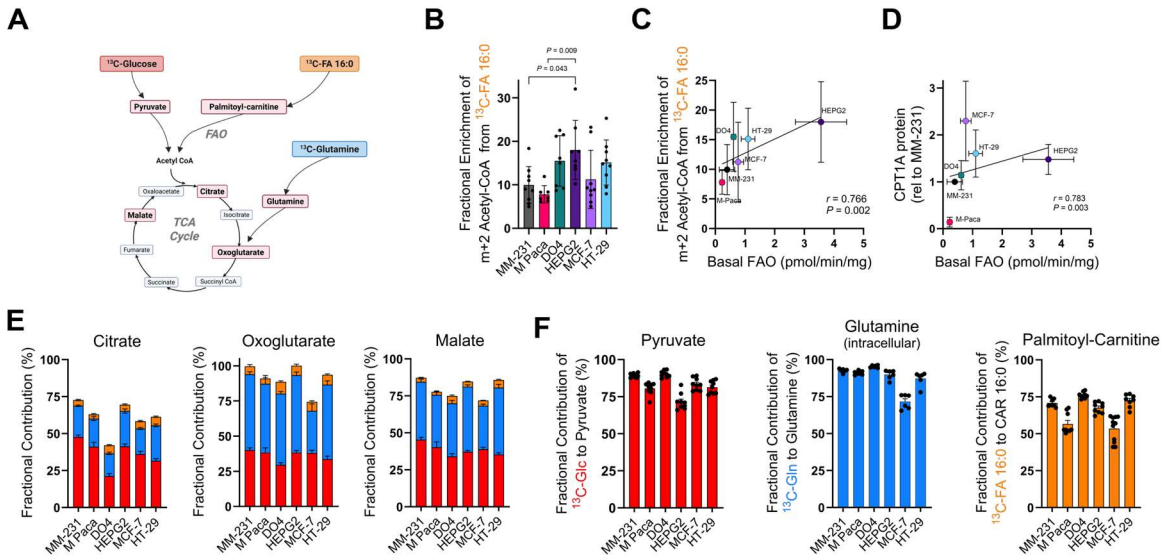

Figure 2. Exogenous fatty acids are minor carbon contributors to the TCA cycle compared to glucose and glutamine, irrespective of oxidative capacity.

(A) Schematic representation of [U-^{13}C]-glucose (5 mM), glutamine (1 mM), or FA 16:0 (150 µM) tracing into the TCA cycle and precursor metabolite.
(B) Fractional contribution of [U-^{13}C]-FA 16:0 to m+2 acetyl-CoA after 6 hours of labelling. N=9 per cell line.
(C) Correlation between [U-^{13}C]-FA 16:0 to m+2 acetyl-CoA and basal FAO rate. Error bars represent ± SD. *P* and *r* values by linear regression.
(D) Correlation between CPT1a protein levels and basal FAO rate. Error bars represent ± SD. *P* and *r* values by linear regression.
(E) Fractional contributions of [U-^{13}C]-glucose (red), glutamine (blue), or FA 16:0 (orange) to citrate, oxoglutarate, and malate. N=9 per cell line.
(F) Fractional contribution of [U-^{13}C]-glucose to pyruvate (red), [U-^{13}C]-glutamine to intracellular glutamine (blue), [U-^{13}C]-FA 16:0 to palmitoyl-carnitine (orange) after 6 hours of labelling. N=9 per cell line. Level of natural enrichment of metabolite standards indicated.

Graphs show mean ± SEM unless stated otherwise. ^{13}C-FA 16:0: U-^{13}C-palmitate; MM-231: MDA-MB-231; M-Paca: Mia Paca-2. See also Figure S2.

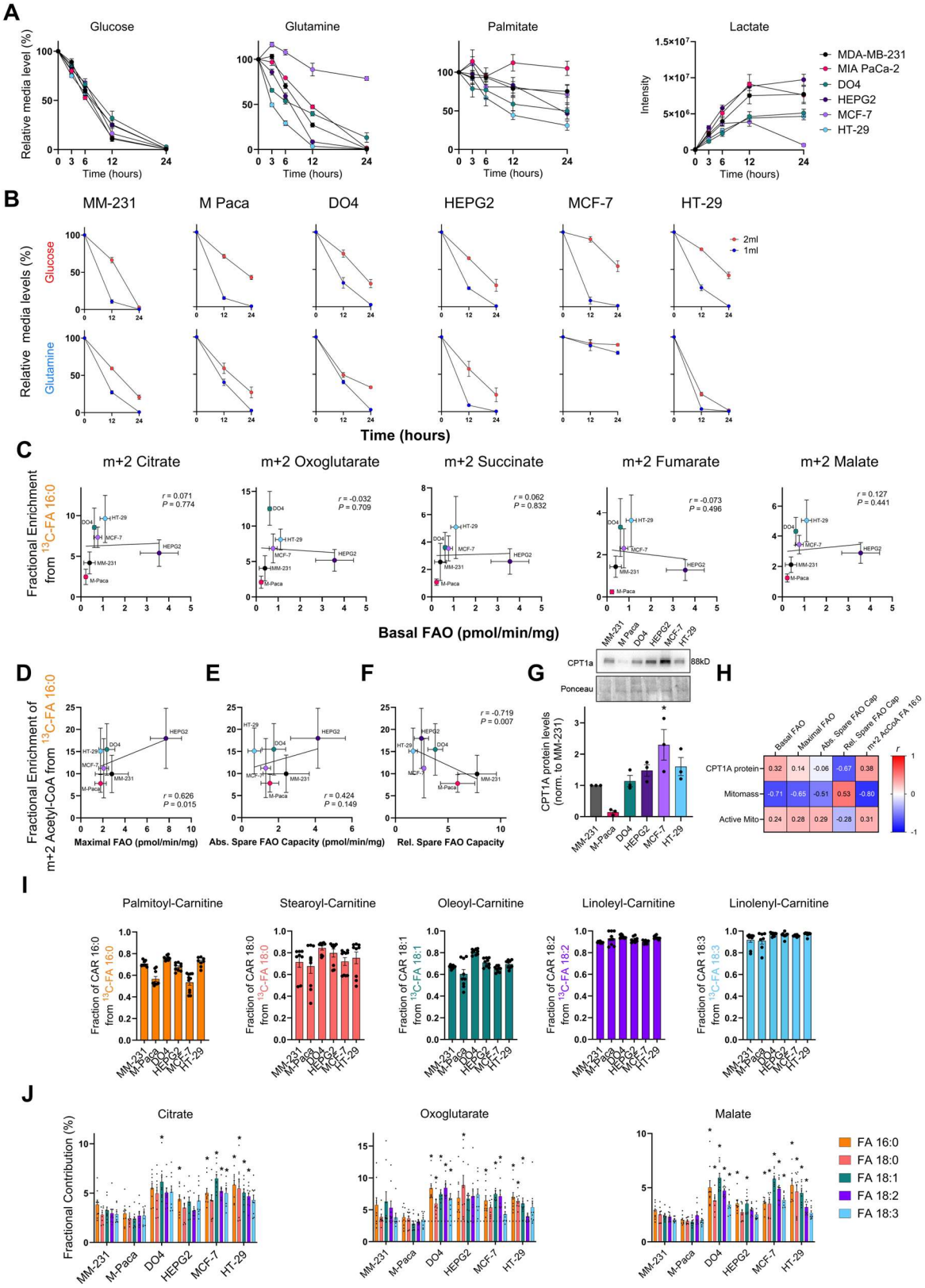
A
Glucose
Glutamine
Palmitate
Lactate
Relative media level (%)
Intensity
Time (hours)
MDA-MB-231
MIA PaCa-2
DO4
HEPG2
MCF-7
HT-29
B
MM-231
M Paca
DO4
HEPG2
MCF-7
HT-29
Relative media levels (%)
Glucose
Glutamine
2ml
1ml
Time (hours)
C
m+2 Citrate
m+2 Oxoglutarate
m+2 Succinate
m+2 Fumarate
m+2 Malate
Fractional Enrichment from 13C-FA 16:0
r = 0.071
P = 0.774
r = -0.032
P = 0.709
r = 0.062
P = 0.832
r = -0.073
P = 0.496
r = 0.127
P = 0.441
Basal FAO (pmol/min/mg)
D
E
F
G
H
Fractional Enrichment of m+2 Acetyl-CoA from 13C-FA 16:0
r = 0.626
P = 0.015
r = 0.424
P = 0.149
r = -0.719
P = 0.007
Maximal FAO (pmol/min/mg)
Abs. Spare FAO Capacity (pmol/min/mg)
Rel. Spare FAO Capacity
CPT1a
88kD
Ponceau
CPT1A protein levels (norm. to MM-231)
Basal FAO
Maximal FAO
Abs. Spare FAO Cap
Rel. Spare FAO Cap
m+2 AcCoA FA 16:0
CPT1A protein
Mitomass
Active Mito
I
Palmitoyl-Carnitine
Stearoyl-Carnitine
Oleoyl-Carnitine
Linoleyl-Carnitine
Linolenyl-Carnitine
Fraction of CAR 16:0 from 13C-FA 16:0
Fraction of CAR 18:0 from 13C-FA 18:0
Fraction of CAR 18:1 from 13C-FA 18:1
Fraction of CAR 18:2 from 13C-FA 18:2
Fraction of CAR 18:3 from 13C-FA 18:3
J
Citrate
Oxoglutarate
Malate
Fractional Contribution (%)
FA 16:0
FA 18:0
FA 18:1
FA 18:2
FA 18:3

213

Figure S2, related to figure 2. Kinetic profiling of substrate uptake and lack of correlation between mitochondrial mass and FAO capacity.

(A) Media glucose, glutamine, FA 16:0 (palmitate) levels relative to t = 0, and lactate intensity over 24 hours. N=3 per cell line.
(B) Media glucose or glutamine levels over 24 hours relative to t = 0 from wells containing 1 mL (blue) or 2 mL (red) of medium. N=3 per cell line. Graphs show mean ± SEM
(C) Fractional contribution of [U-^{13}C]-FA 16:0 to m+2 TCA cycle metabolites after 6 hours of labelling. N=9 per cell line. Level of natural enrichment of metabolite standards indicated. Graphs show mean ± SD. *P* and *r* values by linear regression.
(D) Correlation between [U-^{13}C]-FA 16:0 to m+2 acetyl-CoA and maximal FAO rate (glucose-free media). Error bars represent ± SD. *P* and *r* values by linear regression.
(E) Correlation between [U-^{13}C]-FA 16:0 to m+2 acetyl-CoA and absolute spare FAO rate (Maximal FAO – Basal FAO). Error bars represent ± SD. *P* and *r* values by linear regression.
(F) Correlation between [U-^{13}C]-FA 16:0 to m+2 acetyl-CoA and relative spare FAO rate (Maximal FAO / Basal FAO). Error bars represent ± SD. *P* and *r* values by linear regression.
(G) Representative immunoblots and densitometric quantitation of CPT1a.
(H) Correlation matrix of measures of FAO capacity and CPT1 protein level, and mitochondrial mass (using MitoTracker Green) and mitochondrial membrane potential (Active Mito; using MitoTracker Red). *r* values by linear regression.
(I) Fractional contributions of [U-^{13}C]- FA 16:0 (palmitate), 18:0 (stearate), 18:1 (oleate), 18:2 (linoleate), and 18:3 (linolenate) to acyl-carnitine species. N=9 per cell line.
(J) Fractional contributions of [U-^{13}C]- FA 16:0 (palmitate), 18:0 (stearate), 18:1 (oleate), 18:2 (linoleate), and 18:3 (linolenate) to citrate, oxoglutarate, and malate. N=9 per cell line.

Graphs show mean ± SEM unless stated otherwise. ^{13}C-FA 16:0: U-^{13}C-palmitate; MM-231: MDA-MB-231; M-Paca: Mia Paca-2.

Fatty acid oxidation compensates for reduced glucose-derived acetyl-CoA in the mitochondrial pool.

Given the extensive interest in FAO in cancer [28-31], and our observations that FAO is not a major carbon source for fuelling the TCA cycle, we sought to gain new insights into how cancer cells integrate mitochondrial metabolic activity in our panel of cancer cell lines with varying FAO capacity. We first focused on glucose metabolism, given the seminal work of Randle and colleagues [32], which showed the interaction between fatty acid and glucose metabolism [32], their shared input into the mitochondrial acetyl-CoA pool, and the relationship between glucose availability and FAO rates (Figure 1 and S1). Cells with high basal and maximal FAO rates had higher glucose exclusion, as indicated by m+0 (Figure 3A), and lower m+2 acetyl-CoA (Figure 3B) labelling from [U-^{13}C]-glucose, indicating reduced glucose-derived acetyl-CoA synthesis. This relationship between FAO rate and glucose contribution to acetyl-CoA was supported by very strong negative correlations between the contribution of palmitate and glucose to m+2 acetyl-CoA (r = -0.98; Figure 3C), which was also observed in cells cultured with [U-^{13}C]-stearate (r = -0.95; Figure 3D), oleate (r = -0.76; Figure 3E), linoleate (r = -0.89; Figure 3F), or linolenate (r = -0.97; Figure 3G). These data indicate that in cells where glucose contributes less to acetyl-CoA, fatty acid-derived carbons proportionally contribute more, consistent with a compensatory relationship between these substrates at the level of the acetyl-CoA pool. This inverse relationship between the contribution of glucose and fatty acid to acetyl-CoA was also evident in citrate (m+2; r = -0.43; Figure 3H), but not in m+2 labelling of oxoglutarate (Figure 3I), succinate (Figure 3J), fumarate (Figure 3K) or malate (Figure 3L). Overall, we observe a Randle Cycle-like relationship between glucose and fatty acid metabolism at acetyl-CoA in our panel of cancer cells, but this was not propagated through TCA cycle intermediates downstream of glutamine entry. Further, these data support a model in which low glucose-derived acetyl-CoA is compensated by FAO, rather than FAO being the primary driver of glucose suppression

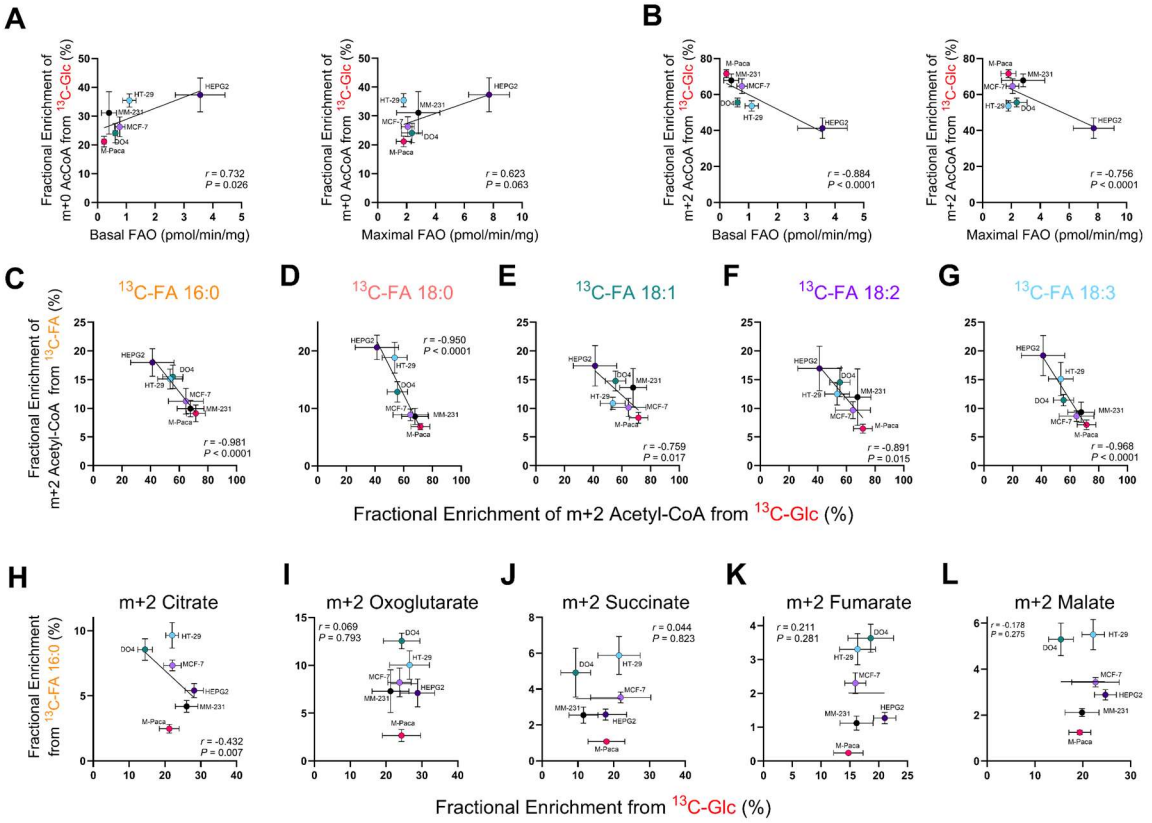

Figure 3. Fatty acid oxidation compensates for reduced glucose-derived acetyl-CoA, consistent with the Randle Cycle.

(A) Correlation between m+0 acetyl-CoA in cells cultured in 5 mM [U-^{13}C]-glucose and basal (left) and maximal (right) FAO rates.
(B) Correlation between m+2 acetyl-CoA in cells cultured in 5 mM [U-^{13}C]-glucose and basal (left) and maximal (right) FAO rates.
(C) Correlation between [U-^{13}C]-FA 16:0 (palmitate) and [U-^{13}C]-glucose contributions to m+2 acetyl-CoA.
(D) Correlation between [U-^{13}C]-FA 18:0 (stearate) and [U-^{13}C]-glucose contributions to m+2 acetyl-CoA.
(E) Correlation between [U-^{13}C]-FA 18:1 (oleate) and [U-^{13}C]-glucose contributions to m+2 acetyl-CoA.
(F) Correlation between [U-^{13}C]-FA 18:2 (linoleate) and [U-^{13}C]-glucose contributions to m+2 acetyl-CoA.
(G) Correlation between [U-^{13}C]-FA 18:3 (linolenate) and [U-^{13}C]-glucose contributions to m+2 acetyl-CoA.
(H) Correlation between [U-^{13}C]-FA 16:0 and [U-^{13}C]-glucose contributions to m+2 citrate.
(I) Correlation between [U-^{13}C]-FA 16:0 and [U-^{13}C]-glucose contributions to m+2 oxoglutarate.
(J) Correlation between [U-^{13}C]-FA 16:0 and [U-^{13}C]-glucose contributions to m+2 succinate.
(K) Correlation between [U-^{13}C]-FA 16:0 and [U-^{13}C]-glucose contributions to m+2 fumarate.
(L) Correlation between [U-^{13}C]-FA 16:0 and [U-^{13}C]-glucose contributions to m+2 malate.

Graphs show mean ± SD. *P* and *r* values by linear regression. ^{13}C-FA 16:0: U-^{13}C-palmitate; ^{13}C-Glc: U-^{13}C-glucose; MM-231: MDA-MB-231; M-Paca: Mia Paca-2.

A compensatory 'dual-fuel' shunt recruits glutamine to maintain acetyl-CoA availability in high-FAO phenotypes.

Having established that higher FAO rates are associated with reduced glucose-derived acetyl-CoA labelling (consistent with a Randle cycle-like relationship at the acetyl-CoA node), which does not extend into TCA cycle intermediates, we next investigated the relationship between FAO and glutamine metabolism (Figure 4A). In striking contrast to the glucose data, cancer cells with high FAO rates exhibited significantly higher glutamine oxidation rates, as evidenced by a strong positive correlation with m+4 succinate from ^{13}C-glutamine (r = 0.90; Figure 4B). This positive coupling was consistent across all metrics of FAO potential, including maximal FAO capacity (r = 0.88; Figure 4C), and absolute FAO spare capacity (e.g. maximal FAO – basal FAO, r = 0.75; Figure S4A), but not relative spare FAO capacity (e.g. maximal FAO/basal FAO ratio; Figure S4B). There was also a coupling of ^{13}C-palmitate contribution to m+2 acetyl-CoA with m+4 succinate from ^{13}C-glutamine (r = 0.49; Figure 4D). This pattern extended throughout the TCA cycle and downstream amino acids, with significant positive correlations observed between FAO activity and glutamine labelling in fumarate, malate, and aspartate (Figure S4C). These data suggest that, rather than competing for mitochondrial entry, FAO and glutamine oxidation are coordinately upregulated and, as such, predict that high FAO cells exhibit low glutamine reductive carboxylation. Surprisingly, cells with higher FAO rates showed increased glutamine reductive carboxylation (indicated by m+5 citrate (Figure 4E) and m+3 aspartate (Figure S4D)). However, when normalising for oxidative flux, cells with higher FAO rates displayed a reduced relative reliance on reductive carboxylation (lower m+5/m+4 citrate ratio; r = -0.336, P = 0.024; Figure 4F). Therefore, cells with higher FAO and lower glucose oxidation preferentially maintain canonical oxidative glutamine cycling. Notably, these cells did not exhibit altered glucose anaplerosis compared with low FAO cells, and there was no correlation between FAO rates and glucose entry via pyruvate carboxylase (m+3 citrate

308 from ^{13}C-glc; Figure S4E) or between FAO rates and pyruvate partitioning between anaplerosis
309 and cataplerosis (m+3/m+2 citrate from ^{13}C-glc; Figure S4F).

310 What we could not reconcile from these relationships was the absolute carbon contributions to
311 key metabolites, especially to the synthesis of acetyl-CoA and citrate (Figure 2). For example,
312 palmitate contributes only 9-18% of carbon to acetyl-CoA (Figure 2B) and <6% to citrate
313 (Figure 2F) in our panel of cells, whereas glucose contributes 41-72% to acetyl-CoA (Figure
314 3) and 30-50% to citrate (Figure 2F). Notably, in cells with high FAO rates, fatty acids and
315 glucose together accounted for only ~50% of acetyl-CoA labelling, compared with ~80% in
316 low-FAO cells, implying that an additional substrate must sustain acetyl-CoA supply in the
317 high-FAO state. The coupling of FAO and glutamine oxidation and reductive carboxylation
318 Figure 4B-F) raised the prospect that this could extend the acetyl-CoA pool, where glutamine
319 carbons enter the TCA cycle, exit via malic enzyme as pyruvate, and re-enter as acetyl-CoA,
320 effectively backfilling the acetyl-CoA pool when glucose-derived acetyl-CoA is low in high-
321 FAO cells. This concept was supported by a strong positive correlation between basal FAO
322 rates and the contribution of glutamine to acetyl-CoA (m+2; r = 0.91; Figure 4G), which ranged
323 from 9% to 26%. We saw the same positive relationship between FAO rate and glutamine
324 labelling of pyruvate (m+3, r = 0.67; Figure 4H; m+2, r = 0.86; Figure S4G). The enrichment
325 of glutamine-derived pyruvate was predictive of glutamine-derived acetyl-CoA (Figure 4I and
326 S4H). More broadly, this increased enrichment of acetyl-CoA from glutamine in cells with
327 higher FAO was also evident when we quantified the total fractional contribution from
328 glutamine and palmitate (r = 0.968; Figure 4J), whereas there was a negative relationship
329 between glucose enrichment of acetyl-CoA and glutamine (r = -0.966; Figure 4K) and
330 palmitate (r = -0.966; Figure 4L). Collectively, these data reveal a dual-fuel mechanism in high-
331 FAO cancer cells in which fatty acid oxidation and a malic enzyme-dependent glutamine–

pyruvate shunt jointly supplement acetyl-CoA production when glucose-derived acetyl-CoA synthesis is low, while glucose-derived anaplerosis is maintained (Figure 4M).

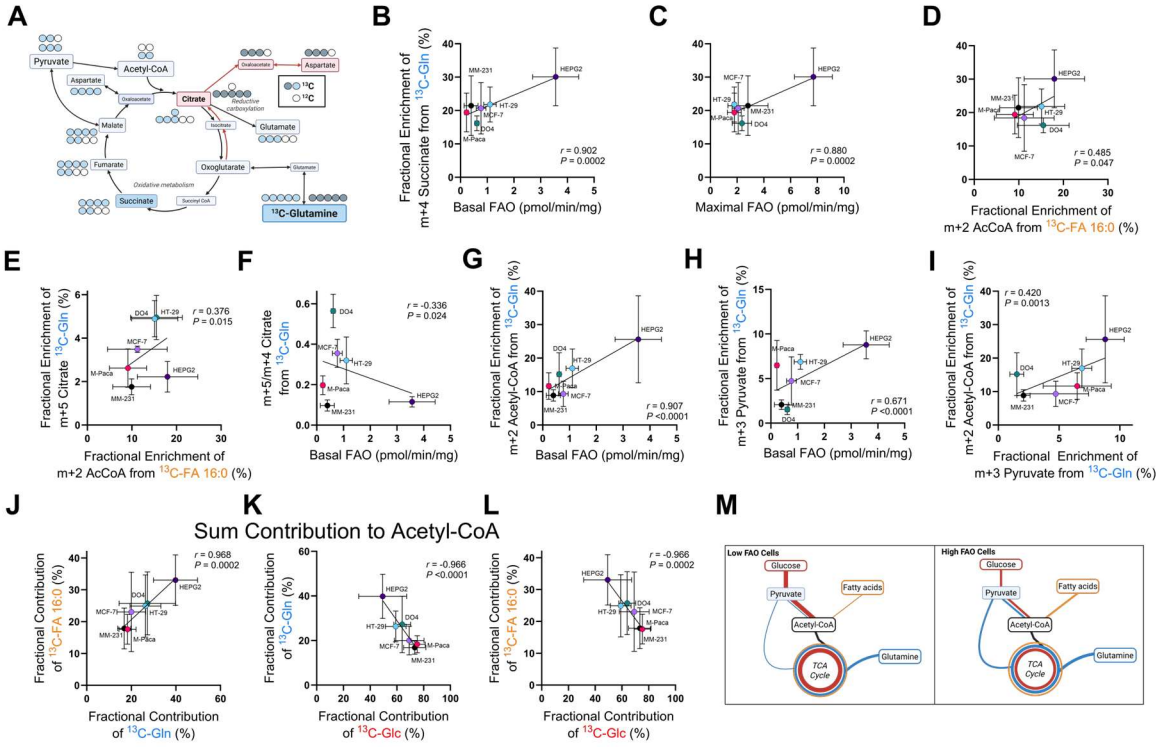

Figure 4. High fatty acid oxidation rates are positively coupled to glutamine metabolism and drive a compensatory dual-fuel shunt to maintain acetyl-CoA.

(A) Schematic of [U-^{13}C]-glutamine (^{13}C-Gln) oxidation and reductive carboxylation.
(B) Correlation between m+4 succinate from glutamine (glutamine oxidation) and basal FAO rate.
(C) Correlation between m+4 succinate from glutamine (glutamine oxidation) and maximal FAO rate.
(D) Correlation between m+4 succinate from glutamine (glutamine oxidation) and m+2 acetyl-CoA from [U-^{13}C]-FA 16:0 (palmitate).
(E) Correlation between m+5 citrate from glutamine (reductive carboxylation) and m+2 acetyl-CoA from [U-^{13}C]-FA 16:0 (palmitate).
(F) Correlation between m+5 citrate / m+4 citrate from glutamine (reductive carboxylation / glutamine oxidation) and basal FAO rate.
(G) Correlation between m+3 pyruvate from glutamine and basal FAO rate.
(H) Correlation between m+2 acetyl-CoA from glutamine and basal FAO rate.
(I) Correlation between m+3 pyruvate and m+2 acetyl-CoA from glutamine.
(J) Correlation between [U-^{13}C]-FA 16:0 and [U-^{13}C]-glutamine to acetyl-CoA.
(K) Correlation between [U-^{13}C]-glutamine and [U-^{13}C]-glucose (^{13}C-Glc) to acetyl-CoA.
(L) Correlation between [U-^{13}C]-FA 16:0 and [U-^{13}C]-glucose to acetyl-CoA.
(M) Schematic of dual-fuel link between FAO and glutamine metabolism to maintain acetyl-CoA levels.

Graphs show mean ± SD. *P* and *r* values by linear regression. ^{13}C-FA 16:0: U-^{13}C-palmitate; ^{13}C-Glc: U-^{13}C-glucose; ^{13}C-Gln: U-^{13}C-glutamine; MM-231: MDA-MB-231; M-Paca: Mia Paca-2. See also Figure S4.

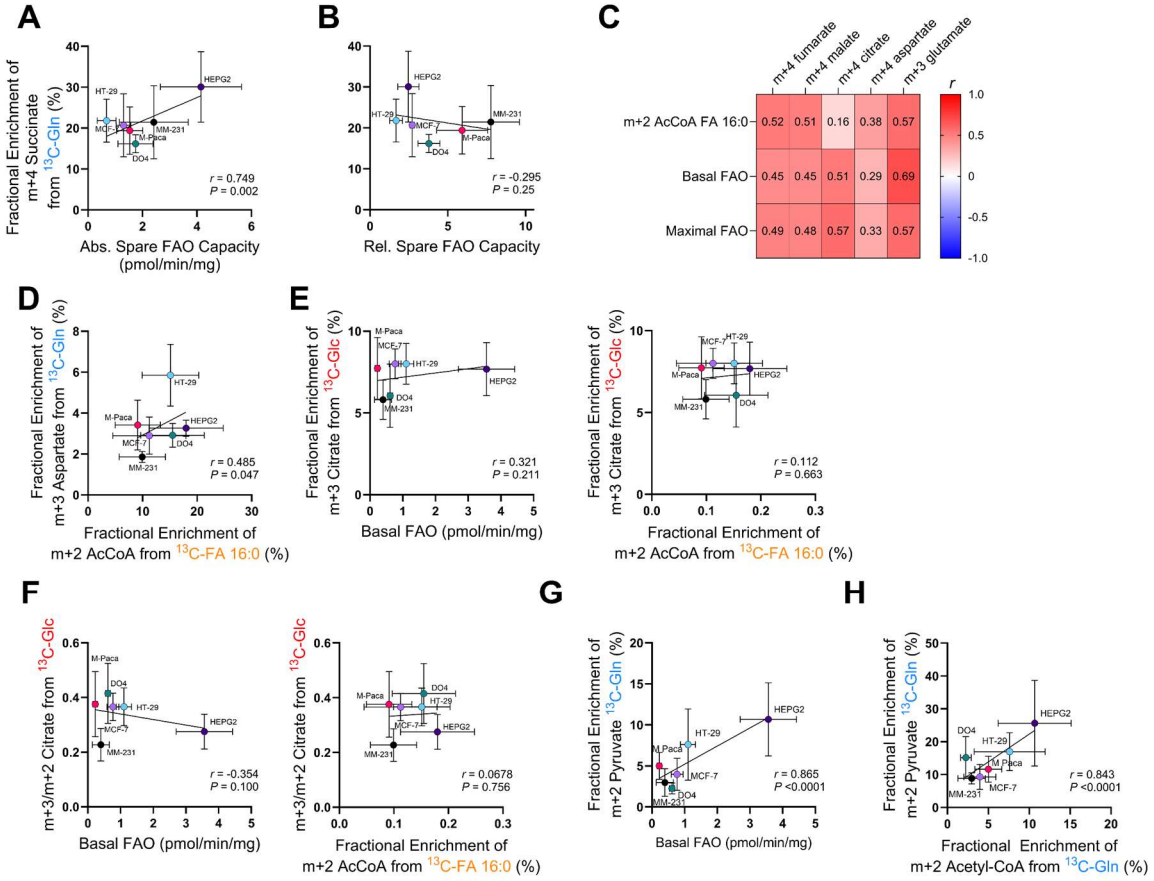

Figure S4, related to figure 4. Relationships between fatty acid oxidation capacity, glutamine metabolism and glucose anaplerotic flux.

(A) Correlation between m+4 succinate from glutamine (glutamine oxidation) and absolute spare FAO rate (Maximal FAO – Basal FAO).
(B) Correlation between m+4 succinate from glutamine and relative spare FAO rate (Maximal FAO / Basal FAO).
(C) Correlation matrix between [U-^{13}C]-glutamine enrichment into m+4 isotopologues of metabolites and measures of FAO.
(D) Correlation between m+3 aspartate from glutamine and m+2 acetyl-CoA from [U-^{13}C]-FA 16:0 (palmitate).
(E) Correlation between m+3 citrate from glucose (anaplerosis) and basal FAO rate (left) and [U-^{13}C]-FA 16:0 to m+2 acetyl-CoA (right).
(F) Correlation between m+3 citrate / m+2 citrate from glucose (anaplerosis / oxidation) and basal FAO rate (left) and [U-^{13}C]-FA 16:0 to m+2 acetyl-CoA (right).
(G) Correlation between m+2 pyruvate from glutamine (2nd turn of TCA cycle of glutamine oxidation) and basal FAO rate.
(H) Correlation between m+2 pyruvate and m+2 acetyl-CoA from glutamine.

Graphs show mean ± SD unless stated otherwise. *P* and *r* values by linear regression. ^{13}C-FA 16:0: U-^{13}C-palmitate; ^{13}C-Glc: U-^{13}C-glucose; ^{13}C-Gln: U-^{13}C-glutamine; MM-231: MDA-MB-231; M-Paca: Mia Paca-2.

372 **High FAO capacity does not confer bioenergetic autonomy under nutrient**
373 **stress.**

374 Having established that FAO is a minor direct carbon source for the TCA cycle and instead
375 supplements acetyl-CoA production alongside glutamine when glucose-derived acetyl-CoA
376 synthesis is low, we next asked whether this compensatory role is fixed or conditional.
377 Specifically, we questioned whether the low fractional contribution of fatty acids (<10%) in
378 nutrient-replete conditions reflects an actively maintained metabolic configuration that can be
379 overridden when glucose and glutamine are scarce, or whether it reveals a fundamental
380 limitation of the cancer mitochondrial architecture. If FAO truly operates as a reserve fuel
381 source, then deprivation of glucose and glutamine would be expected to force a switch to fatty
382 acid dependence, converting the high FAO enzymatic capacity observed in our panel (Figure
383 1) into substantial TCA cycle fuelling. To test this, we cultured cells in glucose-free or
384 glucose/glutamine-free conditions. As expected, glucose withdrawal triggered a compensatory
385 upregulation in FAO rates (Figure 1C and 1D) and increased the fractional enrichment of ^{13}C-
386 palmitate into citrate (Figure 5A and 5B), as well as oxoglutarate and malate (Figure S5A).
387 However, this increase was modest; even under extreme nutrient stress, the contribution of
388 palmitate carbons to the TCA cycle rarely exceeded 15%. This increased fuelling of the TCA
389 cycle by FAO in glucose-/glutamine-free conditions was also associated with other metabolic
390 changes. Specifically, we observed an increase in m+2 and, to a greater extent, m+4 labelling
391 of citrate, corresponding to the 1st and 2nd turns of the TCA cycle, respectively (Figure 3C).
392 These results suggest that palmitate-derived carbons undergo multiple rounds of the TCA cycle
393 when glucose or both glucose and glutamine are absent from the culture medium.

394 Another striking shift in palmitate metabolism in glucose-/ glutamine-deprived conditions was
395 the enrichment of the cataplerotic metabolites, glutamate and aspartate (Figure 5A). Under
396 glucose and glutamine replete conditions, the conversion of palmitate carbon into glutamate

397 and aspartate was minimal (~2-6%) (Figure 5D). However, a shift in palmitate carbon
398 utilisation was observed in glucose and glutamine-deprived medium (~10-19%) and to a lesser
399 extent in glucose-deprived medium (~5-14%) (Figure 3D). Overall, these results indicate that
400 cancer cells can increase the catabolic conversion of palmitate into TCA cycle metabolites and
401 amino acids, but only under extreme conditions when extracellular glucose or glucose plus
402 glutamine are unavailable. Crucially, this shift in the labelling and distribution of fatty acid
403 carbons represents a failed rescue.

404 While the fractional contribution of palmitate increased, the absolute abundance of TCA cycle
405 intermediates (citrate, oxoglutarate, and malate) collapsed in glucose/glutamine-deprived
406 conditions (Figure 5E, S3B). This indicates that even when reliance on FAO is forced by
407 nutrient deprivation, fatty acids are inherently insufficient to replenish the TCA cycle.
408 Importantly, these changes preceded the decrease in cell viability between 6 and 24 hours. The
409 metabolic architecture we identified, in which FAO relies on glutamine anaplerosis (the Malic
410 Enzyme shunt) to function, predicts this failure. Specifically, FAO-derived acetyl-CoA
411 accumulates in the absence of an adequate anaplerotic substrate, stalling the TCA cycle and
412 leading to metabolic collapse and cell death (Figure S5C). As such, these findings are consistent
413 with our model, in which FAO can effectively contribute to TCA cycling only when glutamine-
414 and/or glucose-derived anaplerosis is intact.

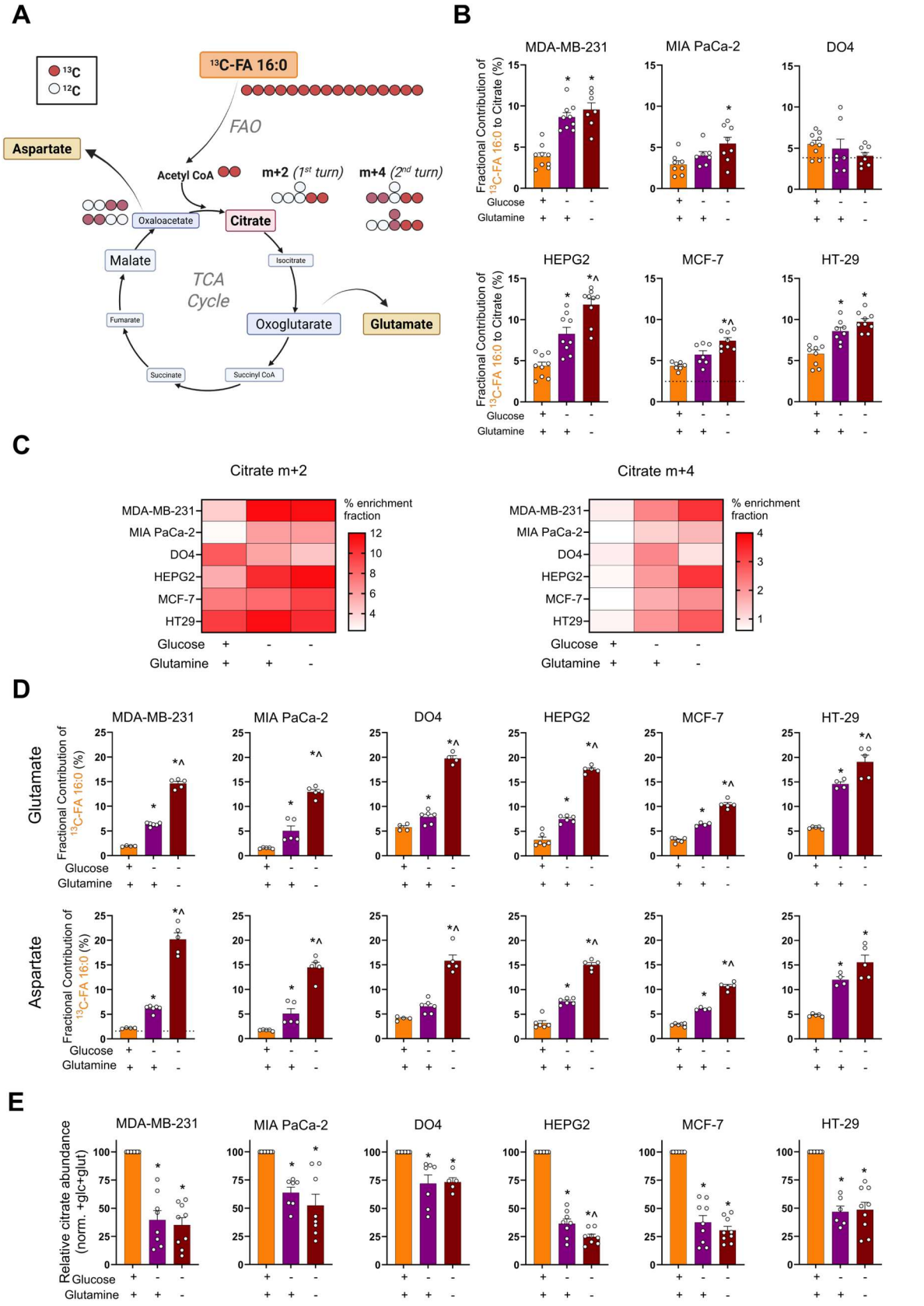
A
13C
12C
13C-FA 16:0
FAO
Aspartate
Acetyl CoA
m+2 (1st turn)
m+4 (2nd turn)
Oxaloacetate
Citrate
Malate
Isocitrate
TCA Cycle
Fumarate
Oxoglutarate
Glutamate
Succinate
Succinyl CoA
B
MDA-MB-231
MIA PaCa-2
DO4
HEPG2
MCF-7
HT-29
Fractional Contribution of 13C-FA 16:0 to Citrate (%)
Glucose
Glutamine
C
Citrate m+2
Citrate m+4
% enrichment fraction
D
Glutamate
Aspartate
Fractional Contribution of 13C-FA 16:0 (%)
E
Relative citrate abundance (norm. +glc+glut)

415

Figure 5. Fatty acid oxidation is insufficient to rescue TCA cycle pool sizes or cell viability in the absence of glucose and glutamine anaplerosis.

(A) Schematic tracing the conversion of [U-^{13}C]-FA 16:0 (palmitate) to citrate m+2 and m+4 glutamate, and aspartate.
(B) Fractional contribution of [U-^{13}C]-FA 16:0 to citrate in cells cultured in +glucose/+glutamine, -glucose/+glutamine, or -glucose/-glutamine. N=9 per cell line.
(C) Enrichment fraction (%) of [U-^{13}C]-FA 16:0 to m+2 and m+4 citrate in cells cultured in + glucose/+glutamine, -glucose/+glutamine, and -glucose/-glutamine. N=9 per cell line.
(D) Fractional contribution of [U-^{13}C]-FA 16:0 to glutamate and aspartate in cells cultured in +glucose/+glutamine, -glucose/+glutamine, or -glucose/-glutamine. N=4-6 per cell line.
(E) Relative abundance of citrate in cells cultured in +glucose/+glutamine, -glucose/+glutamine, or -glucose/-glutamine, normalised to +glucose/+glutamine. N=6-9 per cell line.

Graphs show mean ± SEM. * $P < 0.05$ compared to +glucose/+glutamine, ^ $P < 0.05$ compared to -glucose/+glutamine by One-way ANOVA with Dunnett's multiple comparisons test. See also Figure S5.

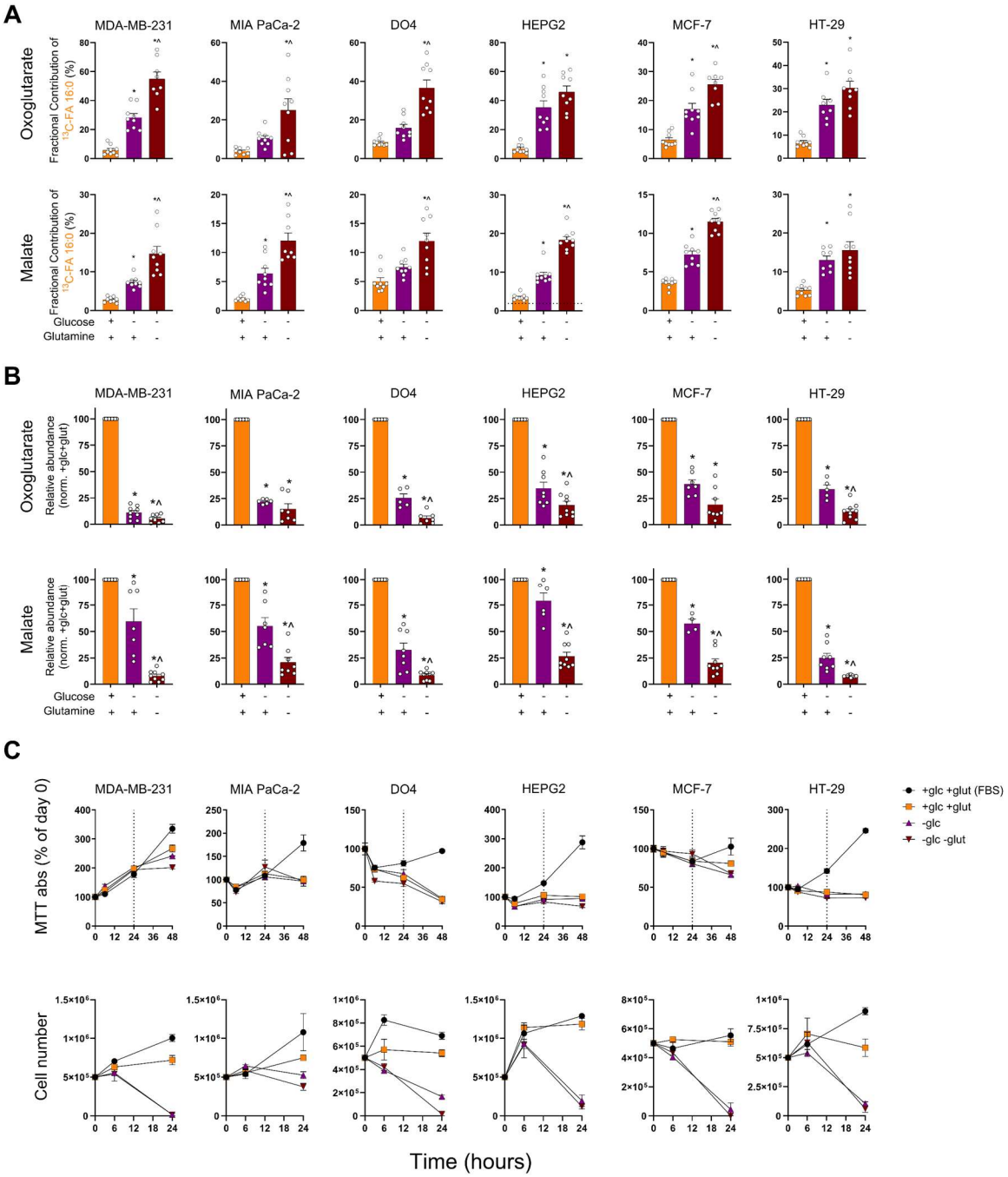

Figure S5, related to figure 5. TCA cycle intermediate abundance and cell viability under nutrient-deprived conditions.

(A) Fractional contribution of [U-^{13}C]-FA 16:0 to oxoglutarate and malate in cells cultured in +glucose/+glutamine, -glucose/+glutamine, or -glucose/-glutamine. N=4-6 per cell line.
(B) Relative abundance (normalised to +glucose/+glutamine) of [U-^{13}C]-FA 16:0 to oxoglutarate or malate. N=5-9 per cell line.
(C) Impact of glucose- or glucose and glutamine- deprivation on metabolic activity (top) assessed by MTT assay. Absorbance results up to 48 hours normalised to day 0 (dotted line at 24 hours indicates replenishment of media); or cell viability (bottom) assessed by live cell counts at 0, 6 and 24 hours. N=3 per group.

Graphs show mean ± SEM. * $P < 0.05$ compared to +glucose/+glutamine, ^ $P < 0.05$ compared to -glucose/+glutamine by One-way ANOVA with Dunnett's multiple comparisons test. Glc: glucose; gln: glutamine.

441 # Discussion

442 Cancer cells display remarkable metabolic plasticity, yet the quantitative contributions of
443 individual fuels to mitochondrial metabolism have been difficult to establish in a comparative,
444 pan-cancer context. While upregulation of FAO and sensitivity to CPT1 inhibition have been
445 taken to imply that fatty acids are major mitochondrial fuels in many malignancies [5,10,26,28-31],
446 yet direct measurements of fatty acid-derived carbon flux relative to glucose and glutamine
447 have been lacking. By combining radiotracer assays, parallel stable-isotope tracing and
448 quantitative mitochondrial phenotyping across 27 cancer cell lines, this study reveals that FAO
449 capacity is profoundly dissociated from FA-derived TCA carbon flux, that FAO participates in
450 a compensatory dual-fuel architecture with glutamine at the acetyl-CoA node, and that FAO
451 cannot rescue TCA cycle activity or viability in the absence of glucose- and glutamine-derived
452 anaplerosis. Understanding the specific contributions of fatty acids relative to glucose and
453 glutamine in cancer metabolism could reveal novel vulnerabilities exploitable for targeted
454 therapies.

455 Stoichiometrically, FAO generates significantly more ATP and reducing equivalents than other
456 oxidative substrates [26,27]. It is through this lens that much of the cancer FAO field has
457 interpreted changes in gene expression and protein levels of those involved in FAO, as well as
458 in vitro measures of fatty acid oxidative activity. For example, increased gene or protein levels
459 of rate-limiting enzymes, or in vitro rates, are often interpreted as increased ATP-generating
460 capacity and likely a dependency. Underpinning these interpretations is the assumption that an
461 increase in capacity (i.e., in vitro flux) leads to greater carbon contribution to the TCA cycle
462 and to more NADH and $FADH_2$ to fuel the electron transport chain. Our results demonstrate a
463 "capacity–contribution paradox" for FAO in cancer. Across a diverse panel of cell lines
464 spanning 10 tissue origins, FAO rates varied by more than 8-fold, yet exogenous LCFAs
465 contributed less than 10% of the carbon to TCA cycle intermediates. This pattern held across

466 multiple FA species. By contrast, glucose and glutamine together accounted for the majority of
467 TCA carbon, in line with their established roles as key mitochondrial fuels in cancer [1-4,33].
468 Whilst basal and maximal FAO rates were related to CPT1A protein levels, cells with faster
469 FAO rates had less mitochondrial mass. Further, spare FAO capacity in cells varied
470 significantly across our panel, with cells that operated at higher basal FAO levels closer to their
471 mitochondrial FAO ceiling and exhibiting limited relative plasticity to increase FAO flux.

472 In contrast, low basal FAO cells retain greater proportional reserve capacity despite lower
473 absolute rates. These differences in FAO capacity and relationships with CPT1A protein levels
474 and mitochondrial mass highlight the dangers in predicting FAO rates and mitochondrial fatty
475 acid metabolic activity using these measures. Our findings necessitate a reinterpretation of
476 prior studies that attributed the anti-tumour effects of CPT1 inhibition solely to blockade of a
477 major fuel source[5,7-9,13-17]. There is strong clinical and preclinical interest in targeting FAO in
478 a range of cancer types (see reviews[29-31]), and this remains well justified. However, the present
479 data indicate that high FAO capacity does not imply that fatty acids supply most of the
480 mitochondrial carbon. FAO cannot sustain TCA cycle activity or viability under conditions in
481 which glucose- and glutamine-derived anaplerotic fluxes are acutely limited. Whilst previous
482 studies have shown that FAO is upregulated when glycolysis is inhibited, or glucose is scarce
483 [24,34,35], thereby suggesting that FAO provides a reserve fuel that can substitute for glucose under
484 stress. Our data show increased FAO rates and fractional ^{13}C palmitate labelling of TCA
485 metabolites under glucose and glucose/glutamine deprivation, with absolute TCA metabolite
486 pools collapsing and leading to reduced cell viability. These results demonstrate that FAO-
487 derived acetyl-CoA can be used productively only when oxaloacetate supply from glucose
488 and/or glutamine anaplerosis is sufficient. When both glucose and glutamine are limiting, FAO-
489 derived acetyl-CoA cannot be efficiently condensed with oxaloacetate, leading to stalling of
490 TCA cycling, depletion of intermediate pools, and increased diversion of fatty acid-derived

491 carbons into cataplerotic products such as glutamate and aspartate. Therefore, FAO appears to
492 support cancer metabolism through mechanisms beyond bulk carbon and ATP provision,
493 including regulation of redox balance, fatty acyl-CoA pools for membrane homeostasis, or
494 signalling lipids [36-38]. Disentangling these non-canonical roles of FAO will be important for
495 refining FAO-targeted therapies.

496 Having eliminated the carbon fuel role of FAO in cancer cells, we sought to reconcile why
497 blocking fatty acid uptake [19,20,23] and metabolism [22,39,40] in mitochondria of cancer cells impacts
498 cell viability. The inverse relationship between glucose- and FA-derived acetyl-CoA-CoA
499 labelling recalls the classical Randle cycle described in muscle and adipose tissue [32], whereby
500 high FAO suppresses PDH activity and thereby glucose oxidation. However, our data do not
501 support this "FAO shuts down glucose oxidation" model. Firstly, glucose-derived anaplerosis
502 via pyruvate carboxylase (m+3 citrate) is preserved across FAO states, indicating that glucose
503 continues to refill TCA intermediates. Secondly, even in high-FAO cells, fatty acids remain
504 minor contributors to TCA carbon, implying that any reduction in glucose-derived acetyl-CoA
505 cannot be fully offset by FAO alone. Thirdly, a 5-fold increase in media fatty acid levels did
506 not increase FAO rates; only lowering exogenous glucose levels to 3 mM or below increased
507 FAO. As such, these observations argue for a reverse Randle Cycle[41], whereby glucose
508 availability and glycolytic flux dictate FAO rates.

509 We and many others have reported interactions between glucose and glutamine metabolism
510 across diverse settings [33,42-45]. These insights have showcased the critical importance of these
511 nutrients in supporting cancer cell proliferation and spread. Here, we identified a compensatory
512 "dual-fuel" architecture at the level of the mitochondrial acetyl-CoA pool, in which constraints
513 on glucose-derived acetyl-CoA are jointly compensated by FAO and a glutamine-dependent
514 malic enzyme shunt. Our data show that high-FAO cells display increased glutamine oxidation

515 (m+4 succinate) and enhanced labelling of downstream TCA intermediates and amino acids,
516 consistent with elevated glutamine flux through canonical oxidative pathways. At the same
517 time, glutamine-derived labelling of pyruvate and acetyl-CoA increases with FAO rate.
518 Specifically, glutamine carbons enter the TCA cycle, pass through to malate, exit via malic
519 enzyme to generate pyruvate, and re-enter as acetyl-CoA. This malic enzyme–dependent shunt
520 aligns with prior observations that glutamine can be flexibly routed to support both anaplerosis
521 and acetyl--CoA supply in various tumour contexts [46-48]. Our results identify this as an attribute
522 of cells with a high FAO metabolic state. This dual-fuel architecture provides an additional
523 mechanistic explanation for the strong glutamine dependence observed in many cancers (see
524 review[49]), yet may be more evident in cells with high FAO. As such, this new interpretation
525 suggests that targeting glutamine metabolism is likely to be particularly effective in tumours
526 with high FAO signatures; alternatively, in cells where FAO and glutamine metabolism
527 cooperate to sustain acetyl-CoA when glucose-derived acetyl-CoA is limited.

528 Several limitations should be considered when interpreting our findings. First, the study
529 focuses on exogenous long-chain fatty acids, glucose, and glutamine, which together account
530 for 40–80% of TCA cycle labelling. Our results do not suggest that endogenous lipids and other
531 nutrients, including branched-chain amino acids, are not important, as they will provide
532 additional carbon[50-53]. Likewise, we used serum-free, FA-free BSA conditions to isolate the
533 contributions of extracellular fatty acids; however, this approach does not fully recapitulate in
534 vivo lipid availability, with its complex makeup of free fatty acids, lipoprotein-contained
535 complex lipids, and those from local stromal sources [50]. Finally, we acknowledge that all
536 experiments were performed in 2D culture under controlled oxygen and nutrient conditions. In
537 tumours, gradients of oxygen, pH, lipids and stromal interactions can modulate cancer cell
538 metabolic activity. Currently, *in vivo* stable isotope tracing of fatty acid metabolism remains a
539 major technical hurdle for the cancer metabolism field, as it requires significant circulating and

540 intracellular precursor labelling that, to date, has been unachievable, especially to be
541 stoichiometrically comparable to those achieved with ^{13}C-glucose (>50% blood/plasma
542 enrichment [54-56]) and ^{13}C-glutamine (30-60% blood enrichment [55,57,58]).

543 In summary, this study provides quantitative evidence that exogenous long-chain fatty acids
544 are minor carbon sources for the TCA cycle in cancer cells, irrespective of FAO capacity.
545 Rather than acting as a primary mitochondrial fuel, FAO participates in a compensatory dual-
546 fuel architecture in which fatty acid oxidation and a malic enzyme-dependent glutamine shunt
547 together supplement acetyl-CoA synthesis when glucose-derived acetyl-CoA is low. The
548 integrative nature of the metabolism of these nutrients is highlighted by the requirement for
549 glucose to provide anaplerotic support, as FAO cannot maintain TCA cycle activity or cell
550 viability in the absence of glucose- and glutamine-derived anaplerotic support. These findings
551 collectively redefine the functional role of FAO in cancer metabolism, provide a mechanistic
552 basis for reinterpretation of therapies targeting CPT1 and other FAO enzymes, and offer a
553 framework for designing combination strategies that exploit the coupling between FAO,
554 glutamine metabolism, and anaplerotic flux.

555 # Methods

556 ## Key resources table

REAGENT or RESOURCE	SOURCE	IDENTIFIER
Antibodies		
Mouse monoclonal anti-CPT1A	Abcam	Cat#Ab128568; RRID: AB_11141632
Rabbit monoclonal anti-GAPDH	Cell Signalling Technology	Cat#2118; RRID: AB_561053
Chemicals, peptides, and recombinant proteins		
Enzalutamide	Selleckchem	Cat#S1250
Etomoxir	Sigma-Aldrich	Cat#C986W52
Lipofectamine RNAiMAX transfection reagent	Thermo Fisher Scientific	Cat#13778075
[1-^{14}C] Palmitic acid	Perkin Elmer	Cat#NEC075H250UC
Palmitic acid	Sigma-Aldrich	Cat#P0500
D-Glucose	Sigma-Aldrich	Cat#273053
L-Glutamine	Gibco	Cat#25030081
Fatty acid free BSA	Bovogen	Cat#BSAS0.10
L-carnitine hydrochloride	Sigma-Aldrich	Cat#C0283
Mitotracker Green	Thermo Fisher Scientific	Cat#M7514
Mitotracker Red	Thermo Fisher Scientific	Cat#M7512
FCCP	Sigma-Aldrich	Cat#SML2959
DTT	Sigma-Aldrich	Cat#D0632
Protease and Phophatase Inhibitor Cocktail, EDTA free	Astral Scientific	Cat#T-2496
Thiazolyl blue tetrazolium bromide MTT reagent	Sigma-Aldrich	Cat#M2128
Linoleic acid	Sigma Aldrich	Cat#L1012
D-Glucose (U-13C6, 99%)	Cambridge Isotope Laboratories, Inc.	Cat#CLM-1396
L-Glutamine (U-13C5, 99%)	Cambridge Isotope Laboratories, Inc.	Cat#CLM-1822-H
Palmitic acid (U-13C16, 98%)	Cambridge Isotope Laboratories, Inc.	Cat#CLM-409
Stearic acid (U-13C18, 98%)	Cambridge Isotope Laboratories, Inc.	Cat#CLM-6990
Linoleic acid (U-13C18, 98%)	Cambridge Isotope Laboratories, Inc.	Cat#CLM-10487
Linolenic acid (U-13C18, 98%)	Cambridge Isotope Laboratories, Inc.	Cat#8386
Critical commercial assays		
Pierce BCA Protein assay kit	Thermo Fisher Scientific	Cat#23225
Immobilon Crescendo Western HRP substrate	Merck Millipore	Cat#WBLUR0500
Experimental models: Cell lines		
MDA-MB-231	ATCC	ATCC HTB-26 RRID: CVCL_0062
MDA-MB-468	ATCC	ATCC HTB-132
MCF7	ATCC	ATCC HTB-22
MDA-MB-134	ATCC	ATCC HTB-23
C4-2B	ATCC	ATCC CRL-3315
PC-3	ATCC	ATCC CRL-1435
22Rv1	ATCC	ATCC CRL-2505 RRID: CVCL_1045
LNCaP	ATCC	ATCC CRL-1740 RRID: CVCL_1379

DU145	A/Prof. Luke Selth, Flinders University	ATCC HTB-81
CWR-AD1	A/Prof. Luke Selth, Flinders University	Nyquist 2013[59], Li 2013[60]
MR42D	Prof. Lisa Butler, SAHMRI	Bishop 2017[61]
HEPG2	A/Prof. Susan McLennan, University of Sydney	Nagarajan 2019[62]
Ishikawa	Prof. Kyle Hoehn, UNSW	RRID: CVCL_2529
MFE296	Prof. Kyle Hoehn, UNSW	RRID: CVCL_1406
MFE319	Prof. Kyle Hoehn, UNSW	RRID: CVCL_2112
U87	Prof. Lenka Munoz, University of Sydney	RRID: CVCL_3429
MIAPACA-2	A/Prof Thomas Grewal, University of Sydney	RRID: CVCL_0428
OVCAR3	A/Prof. David Croucher, Garvan Institute	RRID: CVCL_0465
SKOV3	A/Prof. David Croucher, Garvan Institute	RRID: CVCL_0532
A375	Dr. Lorey Smith, Peter MacCallum Cancer Centre	ATCC CRL-1619 RRIDL CVCL_0132
HT144	Dr. Lorey Smith, Peter MacCallum Cancer Centre	ATCC HTB-63 RRID: CVCL_0318
WM266.4	Dr. Lorey Smith, Peter MacCallum Cancer Centre	ATCC CRL-1676 RRID: CVCL_2765
DO4-M1	Dr. Lorey Smith, Peter MacCallum Cancer Centre	Parmenter 2014[63]
Detroit562	A/Prof Thomas Grewal, University of Sydney	RRID: CVCL_1171
HT29	A/Prof. Kellie Charles, University of Sydney	RRID: CVCL_A8EZ
SW-48	A/Prof. Kellie Charles, University of Sydney	RRID: CVCL_1724
SW-1417	A/Prof. Kellie Charles, University of Sydney	RRID: CVCL_1717
Software and algorithms		
GraphPad Prism V9	GraphPad Software	https://www.graphpad.com/
Image Lab 6.1	Bio-Rad	https://www.bio-rad.com/en-au/product/image-lab-software
FlowJo 2	FlowJo LLC	https://www.flowjo.com/
MATLAB	Mathworks	https://au.mathworks.com/products/matlab.html
MSConvert	N/A	Chambers 2012[64]
MSDial	Riken	http://prime.psc.riken.jp/compms/msdial/main.html
Biorender	Biorender	https://biorender.com/

557

558 # Method details

559 **Cell lines and culture conditions**

560 A panel of 27 adherent cancer cell lines of 10 different origins was used in this study. Cell lines
561 were obtained from both vendors and kindly provided by academic laboratories. Details of
562 culture media (Gibco) can be found in Supplementary Table 1. All culture media were
563 supplemented with 10% fetal bovine serum (Cytiva Hyclone) and 1% penicillin/streptomycin
564 (Gibco). Cells were incubated at 37°C and 5% CO_2.

565 **^{14}C-Radiolabelling**

566 Cells were seeded in technical triplicate in 6-well plates. The next day, the cells were washed
567 in warm PBS and incubated in 600 μL media containing 0.1 mmol/L cold palmitate, [1-^{14}C]
568 palmitate (0.1 μCi/mL; Perkin Elmer) conjugated to 2% (wt/vol) FA-free BSA and 1 mmol/L
569 -carnitine in RPMI or DMEM glucose-free medium (Gibco) for 4 hours. Fatty acid oxidation
570 rates were determined from CO_2 production as previously described[19] in either 0 mM or 5 mM
571 glucose to measure FAO flexibility. Protein content was measured by BCA protein assay and
572 absorbance was read at 540 nm using a Tecan infinite M1000 pro plate reader.

573 **Radiolabelled glucose titration**

574 MDA-MB-231 cells were treated as described above for radiolabelled experiments, and
575 supplemented with 0, 1, 3, 5, 7, 9 11, and 25 mM glucose +/- 10 μM etomoxir. In the selected
576 panel of six cell lines, cells were treated as described above for radiolabelled experiments,
577 supplemented with 0, 1, 3, and 5 mM glucose.

578 **Mitotracker**

579 Cells were seeded in 12-well plates at a density of $2x10^5$ cells/well in RPMI or HG DMEM
580 medium. After 24 hours, cells were washed in warm PBS, trypsinised, and collected in serum-
581 free RPMI medium. The cell suspension was centrifuged at 1500 rpm for 5min in fluorescence-

582 activated cell sorting (FACS) tubes. Cells were subsequently stained with 200 nM Mitotracker
583 Red and Mitotracker Green at 37°C for 30 mins. Additionally, unstained, red only, green only,
584 and 2.5mM FCCP treated cells were included as experimental controls. Cells were centrifuged
585 at 1500 rpm for 5min and fixed with 4% paraformaldehyde at 37°C for 10 mins. Cells were
586 washed with warm PBS, centrifuged at 1500 rpm for 5 mins and resuspended in 150 mL PBS
587 before the samples were read on a BD LSR Fortessa flow cytometer. Data analysis was
588 performed using FlowJo software.

589 **Immunoblotting**

590 Cells were seeded in 6-well plates ($5x10^5$). After 24 hours, cells were lysed in RIPA buffer
591 containing 1% DTT and 0.1% protease and phosphatase inhibitor cocktail. Protein content was
592 measured by BCA protein assay, and absorbance was read at 540 nm using a TECAN infinite
593 M1000 pro plate reader. Cell lysates were subjected to SDS-PAGE, and transferred to
594 polyvinylidene difluoride (PVDF) membranes (Merck Millipore). Ponceau staining was
595 performed on the membranes as a loading control, and then membranes were immunoblotted
596 for CPT1a. Chemiluminescence was performed using Luminata Crescendo Western HRP
597 Substrate and imaged using the Bio-Rad ChemiDoc MP Imaging System and Image Lab
598 software 4.1 (Bio-Rad Laboratories).

599 **Cell viability**

600 Cells were seeded in 96-well plates in 6 well replicates ($3x10^3$ cells/well). After 24 hours the
601 media was removed and replaced with glucose- and glutamine free media (Gibco)
602 supplemented with 5 mM glucose, 1 mM glutamine and/or 150 μM fatty acids, conjugated to
603 2% (wt/vol) FA-free BSA. For glucose-deprived conditions, DMEM no glucose, no glutamine
604 media was supplemented with 1 mM glutamine and 150 μM palmitate; for glucose and
605 glutamine-deprived conditions, media was supplemented with 150 μM palmitate only. Media

606 supplemented with 10% FBS was used as a control. At 6, 12, and 24 hours, 50 µl of MTT
607 reagent was added to each well. MTT reactions were incubated at 37°C and 5% CO_2 for 4
608 hours, and then stopped by replacing the media with 100 µl DMSO (Sigma–Aldrich) per well.
609 Absorbance was read at 540 nm using a TECAN infinite M1000 Pro plate reader. Cells were
610 seeded in 6-well plates at $5x10^5$ cells/well for live cell count. After 24 hours, media was
611 replaced as described for the MTT assay, and the cells counted by trypan blue (Gibco) exclusion
612 at 6 and 24 hours.

613 **[U-^{13}C]-stable isotope tracing**

614 Cells were seeded in 6-well plates ($5x10^5$). After 24 hours, plates were washed with warm PBS
615 and media replaced with 600 µL of no glucose and no glutamine DMEM (Gibco) supplemented
616 with 5 mM glucose, 1 mM glutamine and/or 150 µM FAs, replaced with their respective [U-
617 ^{13}]-C forms. [U-^{13}C]-fatty acids used were palmitate (16:0), oleate (18:0), stearate (18:1),
618 linoleate (18:2), and linolenate (18:3). For glucose-deprived conditions, no glucose and no
619 glutamine DMEM was supplemented with 1 mM glutamine and 150 µM [U-^{13}C]-palmitate;
620 for glucose and glutamine-deprived conditions media was supplemented with 150 µM [U-^{13}C]-
621 palmitate only. Fatty acids were conjugated to 2% (wt/vol) fatty acid-free BSA-containing
622 media for 24 hours at 37 °C before treating cells. Cells were incubated in ^{13}C containing
623 medium for 6 hours.

624 **Extracellular substrate sampling**

625 Cells were seeded in 6-well plates ($5x10^5$). After 24 hours, the wells were washed with warm
626 PBS and media replaced with 1 mL or 2 mL of DMEM with no glucose, no glutamine media
627 supplemented with 5 mM glucose, 1 mM glutamine, and 150 µM fatty acids, conjugated to 2%
628 (wt/vol) FA-free BSA. 100 µL of extracellular media was collected from the wells at 3, 6, 12,
629 and 24 hour timepoints for cells incubated in 1 mL of media, and 12 and 24 hours for cells

630 incubated in 2 mL of media. Media samples were centrifuged at 16,000 x g for 5 mins at 4°C,
631 and the supernatant was collected for subsequent LC-MS analysis.

632 **Cell lysate extraction for LC-MS**

633 Media was aspirated from the plates and the cells washed with 2 mL ice-cold 0.9% (w/v) NaCl.
634 Cells were scraped with 300 μL of extraction buffer, EB, (1:1 LC/MS methanol:water (Optima)
635 + 0.1x internal standards (non-endogenous polar metabolites) and transferred to a 1.5 mL
636 microcentrifuge tube. A further 300 μl of EB was added to the cells and combined in the tube.
637 Next, 600 μL of chloroform (Honeywell) was added before vortexing and incubating on ice for
638 10 mins. Tubes were vortexed briefly and centrifuged at 15,000g for 10 mins at 4°C. The
639 aqueous upper layer was collected and dried without heat using a Savant SpeedVac (Thermo
640 Fisher) for metabolomics LC-MS analysis. The lower layer was collected and dried under
641 nitrogen flow for lipidomic LC-MS analysis.

642 **Measuring stable-isotope labelled metabolites by LC-MS**

643 Dried aqueous upper phase samples were resuspended in 40 mL amide buffer A (20mM
644 ammonium acetate, 20 mM ammonium hydroxide, 95:5 HPLC H_2O: Acetonitrile (v/v)) and
645 vortexed and centrifuged at 15 000 x g for 5 mins at 4°C. 20 mL of supernatant was transferred
646 to HPLC vials containing 20 mL acetonitrile for LCMS analysis of amino acids and glutamine
647 metabolites. The remaining 20 mL of the resuspended sample was transferred to HPLC vials
648 containing 20 mL of LC-MS H_2O for LCMS analysis of glycolytic, pentose phosphate pathway,
649 and TCA cycle metabolites. Amino acids and glutamine metabolites were measured using a
650 Vanquish-TSQ Altis (Thermo) LC-MS/MS system. Analyte separation was achieved using a
651 Poroshell 120 HILIC-Z Column (2.1x150 mm, 2.7 mm; Agilent) at ambient temperature. The
652 pair of buffers used were amide buffer A and 100% acetonitrile (Buffer B), flowed at 200
653 mL/min; injection volume of 5 mL. Glycolytic, pentose phosphate pathway and TCA cycle

654 metabolites were measured using 1260 Infinity (Agilent)-QTRAP6500+ (AB Sciex) LC-
655 MS/MS system. Analyte separation was achieved using a Synergi 2.5 mm Hydro-RP 100A LC
656 Column (100x2 mm) at ambient temperature. The pair of buffers used were 95:5 (v/v)
657 water:acetonitrile containing 10 mM tributylamine and 15 mM acetic acid (Buffer A) and 100%
658 acetonitrile (Buffer B), flowing at 200 mL/min; injection volume of 5 mL. Raw data from both
659 LC-MS/MS systems were extracted using MSConvert[64] and in-house MATLAB scripts.

660 **Measuring extracellular substrates by LC-MS**

661 20 μL of collected extracellular media was mixed with 80 μL water, and vortexed. 10 μL of
662 diluted media was mixed with 90 μL of extraction buffer containing 1:1 (v/v) acetonitrile and
663 methanol + 1x internal standards (non-endogenous standards) at -30°C. The mixture was
664 centrifuged at 12,000xg for 5 min at 4°C and transferred into HPLC vials for LC-MS analysis
665 measured using the Vanquish-TSQ Altis as described above. Raw data from both LC-MS/MS
666 systems were extracted using MSConvert[64] and in-house MATLAB scripts.

667 **Measuring stable isotope labelled lipids by LC-MS**

668 Dried lower phase samples were resuspended in 100 μL 4:2:1 (v/v)
669 isopropanol:methanol:chloroform containing 7.5 mM ammonium formate. Acyl-carnitine
670 lipids were measured using a Thermo Scientific Q-Exactive-HF-X Hybrid Quadrupole
671 Orbitrap LC-MS/MS system. Analyte separation was achieved using an Agilent Poroshell 120,
672 HILIC, 2.1x100 mm, 2.7 μm column. The pair of buffers used were 0.1(v/v)% formic acid and
673 10 mM ammonium formate in H_2O and 0.1(v/v)% formic acid in acetonitrile, flowed at 200
674 μL/min on positive mode. MS1 data was acquired with the following settings: 3.5 kV,
675 capillarity temperature 300°C, 120,000, injection time 100 ms, AGC $1x10^6$, scan range 200-
676 1000. For ddMS2 data acquisition, the following settings were used: top 5, resolution 30,000,
677 200-2000, isolation 1.0m/z, nce 30, AGC target $1x10^3$, intensity threshold $5x10^3$, dynamic

678 exclusion 20s. Raw data from both LC-MS/MS systems were extracted using MSConvert[64]
679 and in-house MATLAB scripts.

680 **Quantification and statistical analysis**

681 Student's t-test, one- or two-way ANOVA with Dunnett's or Tukey's multiple comparisons,
682 and linear regression statistical tests were performed using GraphPad Prism 11.0.0 (GraphPad
683 Software). $P < 0.05$ was considered significant. Data are reported as mean ± standard error of
684 the mean (SEM), standard deviation (SD), or min-max values of at least three independent
685 determinations. Radiolabelling experiments for the expansive cell line panel were of at least
686 one independent determination (N=1-x as indicated in the respective figure legend) with at
687 least 3 technical replicates each. Schematic diagrams were created using Biorender.com
688 software.

689 # Supplementary information

690 ## Supplementary Table 1: Cell line details

Cell line	Cancer type	Culture media (Gibco)
MDA-MB-231	Breast	DMEM HG
MDA-MB-468		RPMI
MCF7		DMEM HG
MDA-MB-134		RPMI
C4-2B	Prostate	RPMI
PC-3		RPMI
22Rv1		RPMI
LNCaP		RPMI
DU145		RPMI
CWR-AD1		RPMI
MR42D		RPMI + 10µM enzalutamide
HEPG2	Liver	DMEM HG
Ishikawa	Endometrial	DMEM HG
MFE296		DMEM HG
MFE319		DMEM HG
U87	Glioblastoma	DMEM HG
MIAPACA-2	Pancreatic	DMEM HG
OVCAR3	Ovarian	RPMI
SKOV3		RPMI
A375	Melanoma	RPMI
HT144		RPMI
WM266.4		RPMI
DO4-M1		RPMI
Detroit562	Head and Neck	DMEM/F12
HT29	Colorectal	DMEM HG
SW-48		DMEM HG
SW-1417		DMEM HG

691

692 # Acknowledgements

693 N.T.S. was supported by the Australian Rotary Health/Rotary Club of Blacktown City 'Mel
694 Grey' PhD scholarship. A.J.H. was supported by a Robinson Fellowship from the University
695 of Sydney. This study was supported by funding from The University of Sydney. We thank the
696 Sydney Mass Spectrometry facility for access to LC-MS instruments; Associate Professor
697 Helen McGuire and the Sydney Cytometry core facility for assistance with MitoTracker
698 experiments; and all collaborators who kindly donated cell lines specified in the Key Resources
699 Table.

700 ## Author contributions

701 Conceptualisation by A.J.H. and L.E.Q. Project administration, visualisation, writing-original
702 draft by N.T.S. Investigation by N.T.S., M.F.H.S., M.G., and A.W. Methodology by L.E.Q.
703 Software by N.T.S., and L.E.Q. Formal analysis by N.T.S, L.E.Q., and A.J.H. Writing-editing
704 & reviewing by N.T.S., L.E.Q., and A.J.H. Funding acquisition, resources by A.J.H.
705 Supervision by A.J.H., and L.E.Q.

706 ## Availability of data and materials

707 All data generated or analysed during this study are included in this published article and its
708 supplementary information files. The datasets generated during the current study are available
709 from the corresponding author upon reasonable request.

710 ## Declaration of interests

711 The authors declare that they have no competing interests.

712 # References:

713 1 Fendt, S. M. 100 years of the Warburg effect: A cancer metabolism endeavor. *Cell*
714 **187**, 3824-3828 (2024). https://doi.org/10.1016/j.cell.2024.06.026

715 2 Demicco, M., Liu, X. Z., Leithner, K. & Fendt, S. M. Metabolic heterogeneity in
716 cancer. *Nat Metab* **6**, 18-38 (2024). https://doi.org/10.1038/s42255-023-00963-z

717 3 Yoo, H. C., Yu, Y. C., Sung, Y. & Han, J. M. Glutamine reliance in cell metabolism.
718 *Exp Mol Med* **52**, 1496-1516 (2020). https://doi.org/10.1038/s12276-020-00504-8

719 4 Corbet, C. & Feron, O. Cancer cell metabolism and mitochondria: Nutrient plasticity
720 for TCA cycle fueling. *Biochim Biophys Acta Rev Cancer* **1868**, 7-15 (2017).
721 https://doi.org/10.1016/j.bbcan.2017.01.002

722 5 Hoy, A. J., Nagarajan, S. R. & Butler, L. M. Tumour fatty acid metabolism in the
723 context of therapy resistance and obesity. *Nat Rev Cancer* **21**, 753-766 (2021).
724 https://doi.org/10.1038/s41568-021-00388-4

725 6 Fendt, S. M., Frezza, C. & Erez, A. Targeting Metabolic Plasticity and Flexibility
726 Dynamics for Cancer Therapy. *Cancer Discov* **10**, 1797-1807 (2020).
727 https://doi.org/10.1158/2159-8290.CD-20-0844

728 7 Lin, H. *et al.* Fatty acid oxidation is required for the respiration and proliferation of
729 malignant glioma cells. *Neuro Oncol.* **19**, 43-54 (2017).
730 https://doi.org/10.1093/neuonc/now128

731 8 Nassar, Z. D. *et al.* Human DECR1 is an androgen-repressed survival factor that
732 regulates PUFA oxidation to protect prostate tumor cells from ferroptosis. *Elife* **9**
733 (2020). https://doi.org/10.7554/eLife.54166

734 9 Padanad, M. S. *et al.* Fatty Acid Oxidation Mediated by Acyl-CoA Synthetase Long
735 Chain 3 Is Required for Mutant KRAS Lung Tumorigenesis. *Cell Rep.* **16**, 1614-1628
736 (2016). https://doi.org/10.1016/j.celrep.2016.07.009

737 10 Qu, Q., Zeng, F., Liu, X., Wang, Q. J. & Deng, F. Fatty acid oxidation and carnitine
738 palmitoyltransferase I: emerging therapeutic targets in cancer. *Cell Death Dis.* **7**,
739 e2226-e2226 (2016). https://doi.org/10.1038/cddis.2016.132

740 11 Fritz, I. B. & Yue, K. T. LONG-CHAIN CARNITINE ACYLTRANSFERASE AND
741 THE ROLE OF ACYLCARNITINE DERIVATIVES IN THE CATALYTIC
742 INCREASE OF FATTY ACID OXIDATION INDUCED BY CARNITINE. *J. Lipid*
743 *Res.* **4**, 279-288 (1963).

744 12 Melone, M. A. B. *et al.* The carnitine system and cancer metabolic plasticity. *Cell*
745 *Death Dis.* **9**, 228 (2018). https://doi.org/10.1038/s41419-018-0313-7

13 Pike, L. S., Smift, A. L., Croteau, N. J., Ferrick, D. A. & Wu, M. Inhibition of fatty acid oxidation by etomoxir impairs NADPH production and increases reactive oxygen species resulting in ATP depletion and cell death in human glioblastoma cells. *Biochim Biophys Acta* **1807**, 726-734 (2011). https://doi.org/10.1016/j.bbabio.2010.10.022

14 Schlaepfer, I. R. *et al.* Lipid Catabolism via CPT1 as a Therapeutic Target for Prostate Cancer. *Mol. Cancer Ther.* **13**, 2361-2371 (2014). https://doi.org/10.1158/1535-7163.mct-14-0183

15 Tirado-Vélez, J. M., Joumady, I., Sáez-Benito, A., Cózar-Castellano, I. & Perdomo, G. Inhibition of fatty acid metabolism reduces human myeloma cells proliferation. *PLoS One* **7**, e46484 (2012). https://doi.org/10.1371/journal.pone.0046484

16 Lin, H. *et al.* Fatty acid oxidation is required for the respiration and proliferation of malignant glioma cells. *Neuro Oncol.* **19**, 43-54 (2016). https://doi.org/10.1093/neuonc/now128

17 Lee, J.-S. *et al.* ATP Production Relies on Fatty Acid Oxidation Rather than Glycolysis in Pancreatic Ductal Adenocarcinoma. *Cancers (Basel)* **12**, 2477 (2020).

18 Samudio, I. *et al.* Pharmacologic inhibition of fatty acid oxidation sensitizes human leukemia cells to apoptosis induction. *J Clin Invest* **120**, 142-156 (2010). https://doi.org/10.1172/JCI38942

19 Balaban, S. *et al.* Extracellular Fatty Acids Are the Major Contributor to Lipid Synthesis in Prostate Cancer. *Mol Cancer Res* **17**, 949-962 (2019). https://doi.org/10.1158/1541-7786.MCR-18-0347

20 Balaban, S. *et al.* Heterogeneity of fatty acid metabolism in breast cancer cells underlies differential sensitivity to palmitate-induced apoptosis. *Mol Oncol* **12**, 1623-1638 (2018). https://doi.org/10.1002/1878-0261.12368

21 Shrestha, R. K. *et al.* ACSM1 and ACSM3 regulate fatty acid metabolism to support prostate cancer growth and constrain ferroptosis. *Cancer Res* (2024). https://doi.org/10.1158/0008-5472.CAN-23-1489

22 Nassar, Z. D. *et al.* Human DECR1 is an androgen-repressed survival factor that regulates PUFA oxidation to protect prostate tumor cells from ferroptosis. *Elife* **9**, e54166 (2020). https://doi.org/10.7554/eLife.54166

23 Nassar, Z. D. *et al.* Fatty Acid Oxidation Is an Adaptive Survival Pathway Induced in Prostate Tumors by HSP90 Inhibition. *Mol Cancer Res* **18**, 1500-1511 (2020). https://doi.org/10.1158/1541-7786.MCR-20-0570

24 Kant, S. *et al.* Enhanced fatty acid oxidation provides glioblastoma cells metabolic plasticity to accommodate to its dynamic nutrient microenvironment. *Cell Death Dis.* **11**, 253 (2020). https://doi.org/10.1038/s41419-020-2449-5

25 van Weverwijk, A. *et al.* Metabolic adaptability in metastatic breast cancer by AKR1B10-dependent balancing of glycolysis and fatty acid oxidation. *Nat Commun* **10**, 2698 (2019). https://doi.org/10.1038/s41467-019-10592-4

26 Carracedo, A., Cantley, L. C. & Pandolfi, P. P. Cancer metabolism: fatty acid oxidation in the limelight. *Nat. Rev. Cancer* **13**, 227-232 (2013). https://doi.org/10.1038/nrc3483

27 Martínez-Reyes, I. & Chandel, N. S. Mitochondrial TCA cycle metabolites control physiology and disease. *Nat Commun* **11** (2020). https://doi.org/10.1038/s41467-019-13668-3

28 Rupert, J., Cao, P. H. A., Frigo, D. E. & Kolonin, M. G. Lipids grease the chain of cancer progression. *Trends Cancer* (2026). https://doi.org/10.1016/j.trecan.2025.11.012

29 Rashed, N., Liu, W. & Luo, X. The role of fatty acid oxidation in the tumor microenvironment: Implications for cancer progression and therapeutic strategies. *Biochim Biophys Acta Rev Cancer* **1880**, 189474 (2025). https://doi.org/10.1016/j.bbcan.2025.189474

30 Lei, Y. *et al.* The role and mechanism of fatty acid oxidation in cancer drug resistance. *Cell Death Discov* **11**, 277 (2025). https://doi.org/10.1038/s41420-025-02554-1

31 Kim, S. Y. Fatty acid addiction in cancer: A high-fat diet directly promotes tumor growth through fatty acid oxidation. *Biochim Biophys Acta Rev Cancer* **1880**, 189428 (2025). https://doi.org/10.1016/j.bbcan.2025.189428

32 Randle, P. J., Garland, P. B., Hales, C. N. & Newsholme, E. A. The glucose fatty-acid cycle. Its role in insulin sensitivity and the metabolic disturbances of diabetes mellitus. *Lancet* **1**, 785-789 (1963). https://doi.org/10.1016/s0140-6736(63)91500-9

33 Quek, L. E. *et al.* Glutamine addiction promotes glucose oxidation in triple-negative breast cancer. *Oncogene* **41**, 4066-4078 (2022). https://doi.org/10.1038/s41388-022-02408-5

34 Raulien, N. *et al.* Fatty Acid Oxidation Compensates for Lipopolysaccharide-Induced Warburg Effect in Glucose-Deprived Monocytes. *Front. Immunol.* **8**, 609 (2017). https://doi.org/10.3389/fimmu.2017.00609

35 Jeon, S. M., Chandel, N. S. & Hay, N. AMPK regulates NADPH homeostasis to promote tumour cell survival during energy stress. *Nature* **485**, 661-665 (2012). https://doi.org/10.1038/nature11066

36 Li, P. L. & Gulbins, E. Bioactive Lipids and Redox Signaling: Molecular Mechanism and Disease Pathogenesis. *Antioxid Redox Signal* **28**, 911-915 (2018). https://doi.org/10.1089/ars.2017.7467

37 Bang, S., Choi, S. H. & Jeong, S. M. Beyond Bioenergetics: Emerging Roles of Mitochondrial Fatty Acid Oxidation in Stress Response and Aging. *Cells* **14** (2025). https://doi.org/10.3390/cells14241956

38 Vasan, K., Werner, M. & Chandel, N. S. Mitochondrial Metabolism as a Target for Cancer Therapy. *Cell Metab* **32**, 341-352 (2020). https://doi.org/10.1016/j.cmet.2020.06.019

39 Blomme, A. *et al.* 2,4-dienoyl-CoA reductase regulates lipid homeostasis in treatment-resistant prostate cancer. *Nat Commun* **11**, 2508 (2020). https://doi.org/10.1038/s41467-020-16126-7

40 Ursini-Siegel, J. *et al.* Elevated expression of DecR1 impairs ErbB2/Neu-induced mammary tumor development. *Mol Cell Biol* **27**, 6361-6371 (2007). https://doi.org/10.1128/MCB.00686-07

41 Wolfe, R. R. Metabolic interactions between glucose and fatty acids in humans. *Am J Clin Nutr* **67**, 519S-526S (1998). https://doi.org/10.1093/ajcn/67.3.519S

42 Santiappillai, N. T. *et al.* Pathway metabolite ratios reveal distinctive glutamine metabolism in a subset of proliferating cells. *Mol Syst Biol*, Accepted 28 March (2025). https://doi.org/10.1101/2024.02.18.580900

43 Kaadige, M. R., Elgort, M. G. & Ayer, D. E. Coordination of glucose and glutamine utilization by an expanded Myc network. *Transcription* **1**, 36-40 (2010). https://doi.org/10.4161/trns.1.1.12142

44 Gebregiworgis, T. *et al.* Glucose Limitation Alters Glutamine Metabolism in MUC1-Overexpressing Pancreatic Cancer Cells. *J Proteome Res* **16**, 3536-3546 (2017). https://doi.org/10.1021/acs.jproteome.7b00246

45 Wang, L. *et al.* Molecular link between glucose and glutamine consumption in cancer cells mediated by CtBP and SIRT4. *Oncogenesis* **7**, 26 (2018). https://doi.org/10.1038/s41389-018-0036-8

46 DeBerardinis, R. J., Lum, J. J., Hatzivassiliou, G. & Thompson, C. B. The biology of cancer: metabolic reprogramming fuels cell growth and proliferation. *Cell Metab* **7**, 11-20 (2008). https://doi.org/10.1016/j.cmet.2007.10.002

848 47 Son, J. *et al.* Glutamine supports pancreatic cancer growth through a KRAS-regulated
849 metabolic pathway. *Nature* **496**, 101-105 (2013). https://doi.org/10.1038/nature12040

850 48 Yang, L. *et al.* Metabolic shifts toward glutamine regulate tumor growth, invasion and
851 bioenergetics in ovarian cancer. *Mol Syst Biol* **10**, 728 (2014).
852 https://doi.org/10.1002/msb.20134892

853 49 Wise, D. R. & Thompson, C. B. Glutamine addiction: a new therapeutic target in
854 cancer. *Trends Biochem Sci* **35**, 427-433 (2010).
855 https://doi.org/10.1016/j.tibs.2010.05.003

856 50 Nagarajan, S. R., Butler, L. M. & Hoy, A. J. The diversity and breadth of cancer cell
857 fatty acid metabolism. *Cancer Metab* **9**, 2 (2021). https://doi.org/10.1186/s40170-020-
858 00237-2

859 51 Koundouros, N. & Poulogiannis, G. Reprogramming of fatty acid metabolism in
860 cancer. *Br. J. Cancer* **122**, 4-22 (2020). https://doi.org/10.1038/s41416-019-0650-z

861 52 Hui, S. *et al.* Quantitative Fluxomics of Circulating Metabolites. *Cell Metab.* **32**, 676-
862 688.e674 (2020). https://doi.org/10.1016/j.cmet.2020.07.013

863 53 Neinast, M., Murashige, D. & Arany, Z. Branched Chain Amino Acids. *Annu. Rev.*
864 *Physiol.* **81**, 139-164 (2019). https://doi.org/10.1146/annurev-physiol-020518-114455

865 54 Maher, E. A. *et al.* Metabolism of [U-13 C]glucose in human brain tumors in vivo.
866 *NMR Biomed* **25**, 1234-1244 (2012). https://doi.org/10.1002/nbm.2794

867 55 Bagga, P. *et al.* Characterization of cerebral glutamine uptake from blood in the
868 mouse brain: implications for metabolic modeling of 13C NMR data. *J Cereb Blood*
869 *Flow Metab* **34**, 1666-1672 (2014). https://doi.org/10.1038/jcbfm.2014.129

870 56 Schnelle, M. *et al.* In vivo [U-(13)C]glucose labeling to assess heart metabolism in
871 murine models of pressure and volume overload. *Am J Physiol Heart Circ Physiol*
872 **319**, H422-H431 (2020). https://doi.org/10.1152/ajpheart.00219.2020

873 57 Patel, R. *et al.* Targeting glutamine metabolism improves sarcoma response to
874 radiation therapy in vivo. *Commun Biol* **7**, 608 (2024).
875 https://doi.org/10.1038/s42003-024-06262-x

876 58 Ma, E. H. *et al.* (13)C metabolite tracing reveals glutamine and acetate as critical in
877 vivo fuels for CD8 T cells. *Sci Adv* **10**, eadj1431 (2024).
878 https://doi.org/10.1126/sciadv.adj1431

879 59 Nyquist, M. D. *et al.* TALEN-engineered AR gene rearrangements reveal endocrine
880 uncoupling of androgen receptor in prostate cancer. *Proc. Natl. Acad. Sci. U. S. A.*
881 **110**, 17492-17497 (2013). https://doi.org/doi:10.1073/pnas.1308587110

882 60 Li, Y. *et al.* Androgen receptor splice variants mediate enzalutamide resistance in
883 castration-resistant prostate cancer cell lines. *Cancer Res.* **73**, 483-489 (2013).
884 https://doi.org/10.1158/0008-5472.Can-12-3630

885 61 Bishop, J. L. *et al.* The Master Neural Transcription Factor BRN2 Is an Androgen
886 Receptor–Suppressed Driver of Neuroendocrine Differentiation in Prostate Cancer.
887 *Cancer Discov.* **7**, 54-71 (2017). https://doi.org/10.1158/2159-8290.Cd-15-1263

888 62 Nagarajan, S. R. *et al.* Lipid and glucose metabolism in hepatocyte cell lines and
889 primary mouse hepatocytes: a comprehensive resource for in vitro studies of hepatic
890 metabolism. *Am J Physiol Endocrinol Metab* **316**, E578-E589 (2019).
891 https://doi.org/10.1152/ajpendo.00365.2018

892 63 Parmenter, T. J. *et al.* Response of BRAF-mutant melanoma to BRAF inhibition is
893 mediated by a network of transcriptional regulators of glycolysis. *Cancer Discov.* **4**,
894 423-433 (2014). https://doi.org/10.1158/2159-8290.CD-13-0440

895 64 Chambers, M. C. *et al.* A cross-platform toolkit for mass spectrometry and
896 proteomics. *Nat. Biotechnol.* **30**, 918-920 (2012). https://doi.org/10.1038/nbt.2377

897

13C-Glucose
13C-FA 16:0
Pyruvate
Palmitoyl-carnitine
FAO
13C-Glutamine
Acetyl CoA
Oxaloacetate
Citrate
Glutamine
Malate
Isocitrate
TCA
Cycle
Fumarate
Oxoglutarate
Succinate
Succinyl CoA
13C-FA 16:0
13C-FA 16:0
13C-Glc
13C-Gln
13C-FA 16:0

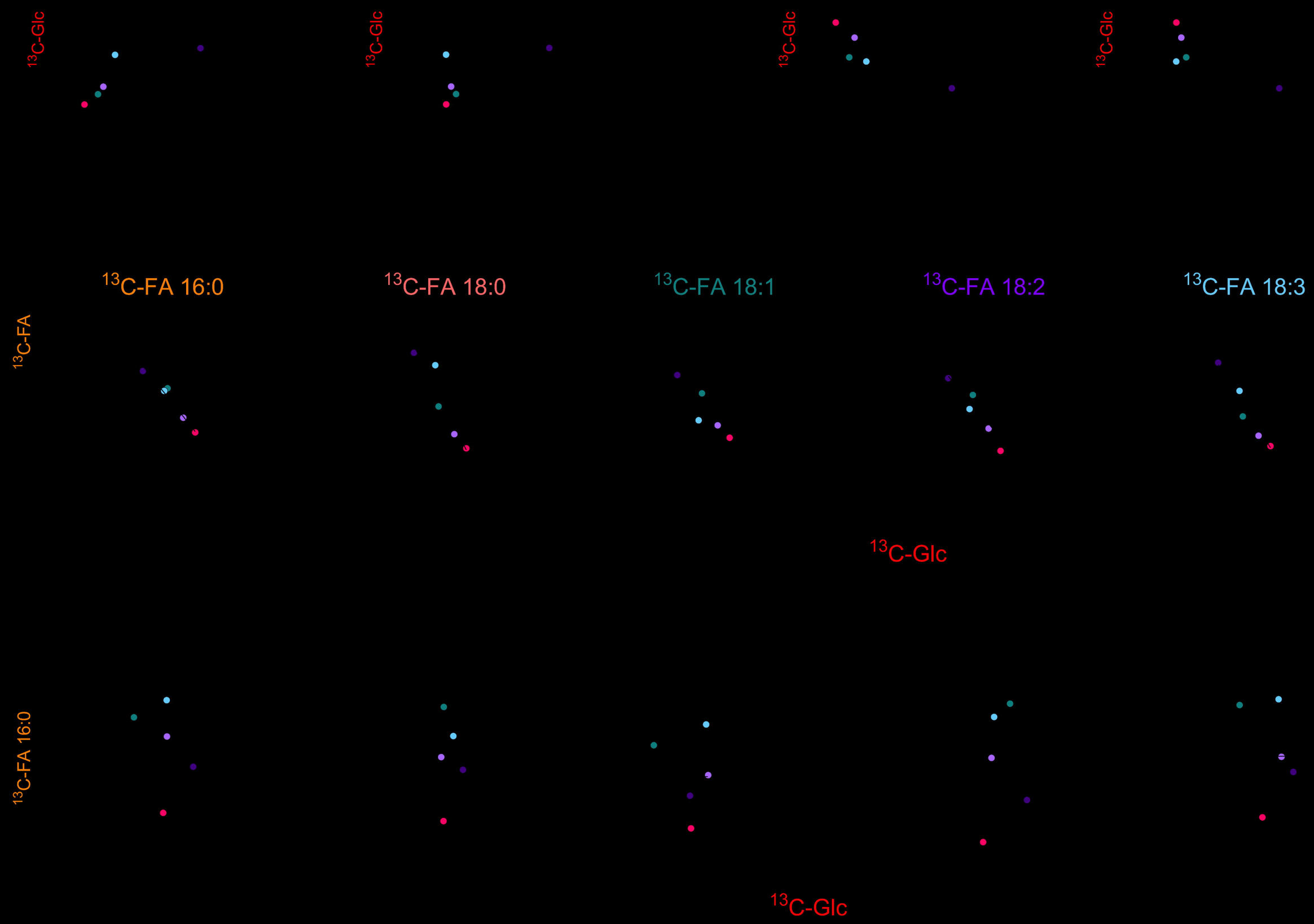
13C-Glc
13C-Glc
13C-Glc
13C-Glc
13C-FA 16:0
13C-FA 18:0
13C-FA 18:1
13C-FA 18:2
13C-FA 18:3
13C-FA
13C-Glc
13C-FA 16:0
13C-Glc

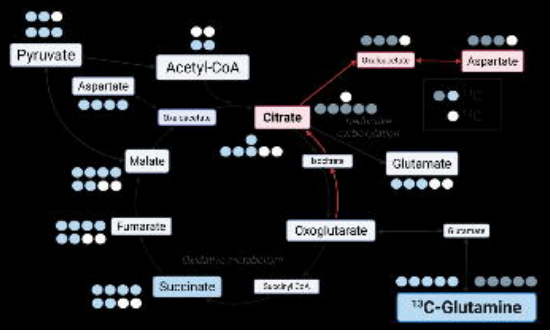
Pyruvate
Acetyl-CoA
Aspartate
Citrate
Aspartate
Malate
Glutamate
Fumarate
Oxoglutarate
Succinate
13C-Glutamine

13C-Gln

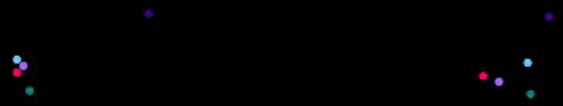

13C-FA 16:0

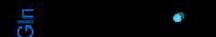
13C-Gln

13C-Gln

13C-Gln

13C-Gln

13C-Gln

13C-FA 16:0

13C-FA 16:0

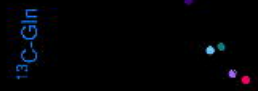
13C-Gln

13C-FA 16:0

13C-Gln

13C-Glc

13C-Glc

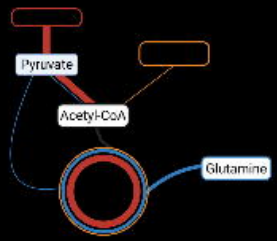
Pyruvate
Acetyl-CoA
Glutamine

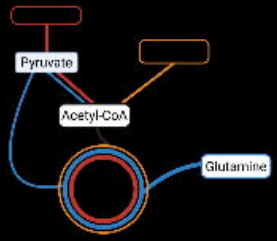
Pyruvate
Acetyl-CoA
Glutamine

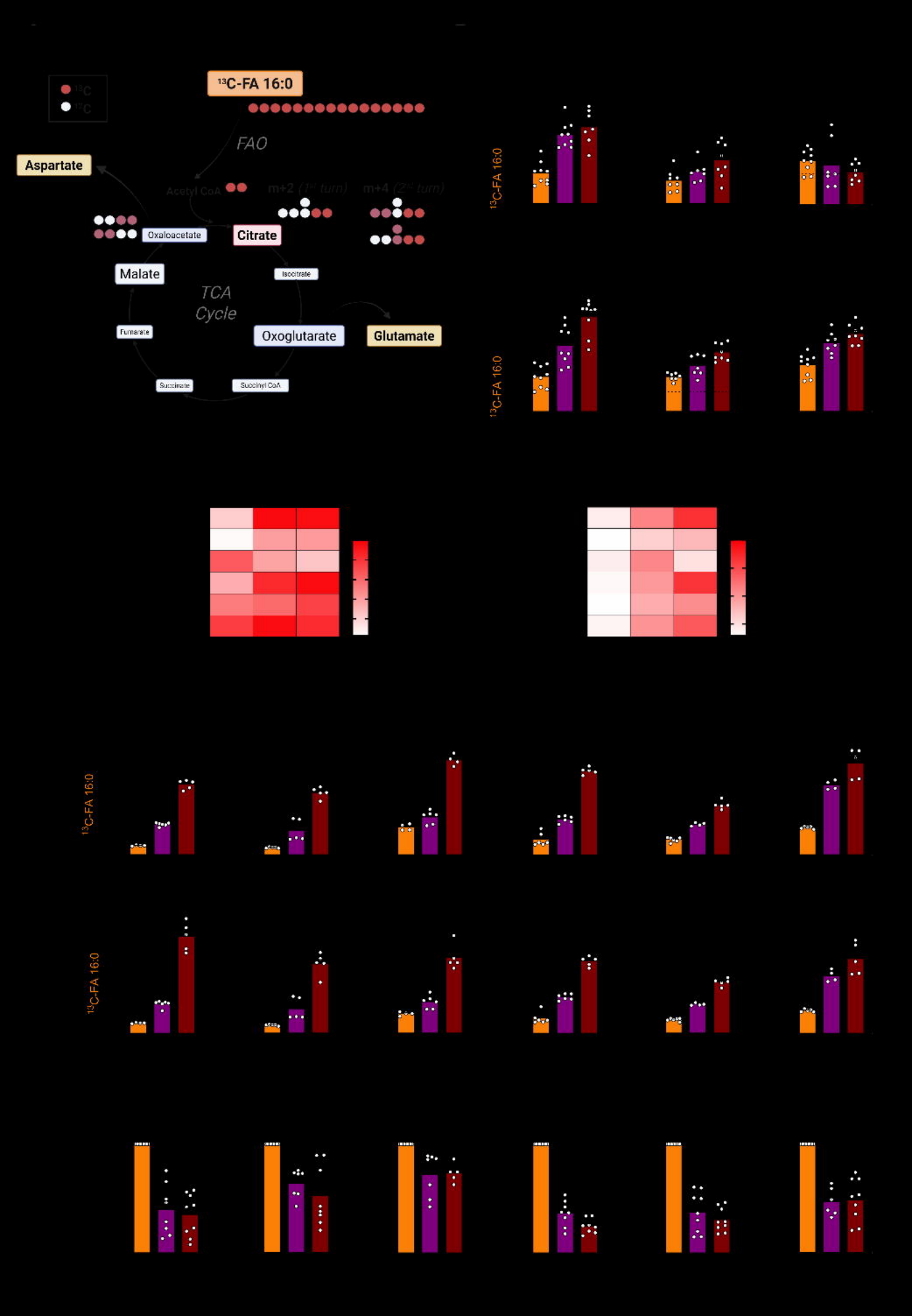
13C
12C
13C-FA 16:0
FAO
Aspartate
Acetyl CoA
m+2 (1st turn)
m+4 (2nd turn)
Oxaloacetate
Citrate
Malate
Isocitrate
TCA Cycle
Fumarate
Oxoglutarate
Glutamate
Succinate
Succinyl CoA
13C-FA 16:0
13C-FA 16:0
13C-FA 16:0
13C-FA 16:0